nature communications

Article

https://doi.org/10.1038/s41467-024-54986-5

A fiducial-assisted strategy compatible with resolving small MFS transporter structures in multiple conformations using cryo-EM

Received: 26 April 2024

Accepted: 24 November 2024

Published online: 02 January 2025

Check for updates

Pujun Xie[1,4], Yan Li[2,4], Gaëlle Lamon[1], Huihui Kuang[3], Da-Neng Wang[2] ✉ & Nathaniel J. Traaseth[1] ✉

Advancements in cryo-EM have stimulated a revolution in structural biology. Yet, for membrane proteins near the cryo-EM size threshold of approximately 40 kDa, including transporters and G-protein coupled receptors, the absence of distinguishable structural features makes image alignment and structure determination a significant challenge. Furthermore, resolving more than one protein conformation within a sample, a major advantage of cryo-EM, represents an even greater degree of difficulty. Here, we describe a strategy for introducing a rigid fiducial marker (BRIL domain) at the C-terminus of membrane transporters from the Major Facilitator Superfamily (MFS) with AlphaFold2. This approach involves fusion of the last transmembrane domain helix of the target protein with the first helix of BRIL through a short poly-alanine linker to promote helicity. Combining this strategy with a BRIL-specific Fab, we elucidated four cryo-EM structures of the 42 kDa *Staphylococcus aureus* transporter NorA, three of which were derived from a single sample corresponding to inward-open, inward-occluded, and occluded conformations. Hence, this fusion construct facilitated experiments to characterize the conformational landscape of NorA and validated our design to position the BRIL/antibody pair in an orientation that avoids steric clash with the transporter. The latter was enabled through AlphaFold2 predictions, which minimized guesswork and reduced the need for screening several constructs. We further validated the suitability of the method to three additional MFS transporters (GlpT, Bmr, and Blt), results that supported a rigid linker between the transporter and BRIL. The successful application to four MFS proteins, the largest family of secondary transporters in nature, and analysis of predicted structures for the family indicates this strategy will be a valuable tool for studying other MFS members using cryo-EM.

Since the Resolution Revolution[1], single particle cryo-electron microscopy (cryo-EM) has become a powerful technique for elucidating biomolecular structures, including macromolecular complexes, membrane proteins, and amyloid fibrils[2–6]. However, a remaining limitation for the technique is the lower size limit of the particles, which has been estimated at ~38 kDa[7]. Two of the largest classes of human membrane proteins are near this size threshold: (i) secondary active transporters from the Major Facilitator Superfamily and (ii)

[1]Department of Chemistry, New York University, New York, NY, USA. [2]Department of Cell Biology, New York University School of Medicine, New York, NY, USA. [3]Cryo-EM Core Laboratory, New York University School of Medicine, New York, NY, USA. [4]These authors contributed equally: Pujun Xie, Yan Li.
✉e-mail: da-neng.wang@med.nyu.edu; traaseth@nyu.edu

G-protein coupled receptors (GPCRs). Proteins within these families often lack extramembrane domains, which leads to challenges in particle alignment in 2D classification and angle determination in 3D classification[8–11]. The results are often low-resolution cryo-EM maps insufficient for constructing atomic resolution models and deciphering molecular mechanisms.

Fiducial-assisted methodologies aim to address these limitations and include synthetic antibodies that bind the target protein and engineered fusion protein constructs[12–14]. The former introduces a recognizable marker and increases the effective size of the system, both of which improve image alignment and enable structure determination[15–17]. An ancillary benefit is increasing the homogeneity of the sample if the binders stabilize a specific conformation. Although this approach has been successfully implemented for transporters and GPCRs[18–21], the discovery of a target-specific binder can be a time-consuming and expensive process. The task becomes even more challenging if one aims to study several conformations as part of the protein's mechanism (e.g., states in a transport cycle). Furthermore, a binder may block access to the binding pocket, preventing structure determination of the protein bound to its substrate or ligand.

To bypass the development of target-specific binders, efforts have focused on protein engineering strategies to accomplish the same goal as binder-assisted methods[22–25]. The challenge for this approach is to constrain the fiducial mark with respect to the target protein. A popular fiducial marker has been the "BRIL" domain from apocytochrome b562a, a four-helix bundle that contains three mutations to stabilize the structure[26]. First utilized as a crystallization chaperone by engineering the domain into the third intracellular loop of GPCRs[27–33], BRIL technology has been further advanced through the discovery of synthetic antibodies that bind BRIL and create a fiducial mark for cryo-EM[34,35]. Several membrane protein structures have benefitted from these developments, including applications to ion channels[36], transporters[37,38], and GPCRs[22,23,39–42]. BRIL has been incorporated into loops adjoining two transmembrane (TM) domains and fused to termini[34,35,39,43–47]. The most successful applications use the former approach where double tethering rigidly couples BRIL to the target protein, enabling structure determination. Fusion of BRIL to the N- or C-terminus would be preferable for reducing chances of protein misfolding and minimizing the potential impact on the target protein's conformation. Yet, there are limited successful examples yielding cryo-EM structures applied to small transporters[38] and no systematic design criteria for achieving a rigid fusion construct. Most studies have relied on trial and error with a few recent examples employing AlphaFold2 for designing suitable constructs[22,23,42,48].

In this work, we describe a design approach to solve structures of small membrane protein transporters from the Major Facilitator Superfamily, the largest family of secondary active transporters in nature[49,50], by rigidly fusing BRIL to the C-terminal end of the target protein. Transporters from this family are involved in a broad range of substrate transport, including movement of ions, metabolites, peptides, and drugs across the membrane through antiport, symport, and uniport mechanisms[49–51]. We demonstrate the suitability of our fusion strategy for cryo-EM studies to four MFS transporters, including structure determination for the 42 kDa transporter NorA.

Results

Design of a fusion protein separated with a rigid linker

Transporters from the Major Facilitator Superfamily (MFS) are commonly comprised of 12 TM domain α-helices[51]. Using this family as the model system, we hypothesized that creation of a continuous helix spanning from TM12 of the transporter to the first helix of the four-helix bundle BRIL domain would result in a sufficiently rigid construct for cryo-EM structure determination (Fig. 1a). Another reason to choose the C-terminus of the transporter as the fusion location is that the last TM helix is far away from the substrate binding site and does not play a major role in substrate recognition or translocation[50].

To test the idea, we initially designed constructs of the *S. aureus* transporter NorA, an MFS protein with 12 TM helices which is involved in antibiotic resistance[52,53]. The first step in the design was to identify residues on the C-terminal end of NorA to be truncated since both AlphaFold2[48] and the experimental structures[18,54] supported the presence of a disordered terminus (Fig. 1a). By using AlphaFold2, we applied the following selection criteria summarized in Fig. 1b to identify the last native residue to retain: (1) the residue possessed a helical secondary structure, (2) the residue made inter-helical structural contacts within 5 Å to a nearby TM helix (or helices), and (3) the residue displayed an AlphaFold2 pLDDT confidence score of 70 or higher (i.e., a "confident" prediction). Based on our selection criteria, Arg380 in TM12 was identified as the last native residue of NorA to retain due to its α-helical secondary structure, packing with residues in TM9 and TM10, and the AlphaFold2 pLDDT score of 82.83. C-terminal residues Ala381 to Met388 were viewed as dispensable to NorA's overall structure since they displayed no contacts to nearby TM helices, did not possess a predicted helical secondary structure, or displayed a pLDDT score below 70. Although it was not essential in the design, our prior cryo-EM maps of NorA also revealed sparse density for these residues[18], supporting the metrics for identifying flexible residues from the AlphaFold2 prediction.

We considered four fusion protein sequences to connect NorA and BRIL, which differed only in the linker's length, ranging from zero to three alanine residues, and allowing the BRIL domain to cover a 360° span of orientations (Fig. 1a). Note that alanine was used previously as a linker for cryo-EM studies[34] and was selected due to its helix inducing properties[55–57]. Furthermore, while other residues also possess helical propensity, alanine has the lowest potential side chain conformational entropy penalty of such residues and given the small size of the side chain it is least likely to make clashes with residues on the target protein. Use of zero to three residues in the linker ensured the BRIL helical bundle resided at four different orientations for selecting a construct that reduced clash with the transporter, particularly if a BRIL-specific Fab was required for structure determination.

Next, AlphaFold2 was used to predict the NorA-BRIL fusion protein structures (Fig. 1c). Analysis of these models aimed to identify a construct with minimal steric clash between NorA, BRIL, and a Fab developed to bind BRIL (BAG2)[34]. The latter was developed as a fiducial marker for cryo-EM and was included in the analysis to increase the size of the complex from 54 kDa to 106 kDa in the instance BRIL was too small to be characterized by cryo-EM. While BAG2 was not included in the AlphaFold2 predictions, its positions were obtained by overlaying BRIL in the BRIL-BAG2 crystal structure (PDB ID: 6CBV)[34] with BRIL in the NorA-BRIL AlphaFold2 predictions. In each highest ranked prediction, NorA resided in the inward-facing conformation and the relative orientation between NorA and BRIL was altered in the expected manner based on the periodicity of the helix.

NorA-BRIL with a three alanine residue linker (NorA-BRIL^{3A}) was identified as the most suitable candidate since it displayed minimal steric interference between NorA and the BRIL/BAG2 pair (Fig. 1c). Given the extended position of BAG2 away from NorA, we also predicted little clash with NorA if it occupied an outward-facing conformation required for its rocker-switch mechanism[51,58], which the highest ranked AlphaFold2 predictions did not consider. Furthermore, we anticipated this orientation of BAG2 relative to NorA would lead to better particle angular alignment since it introduced a more distinguishable fiducial mark. In contrast to the NorA-BRIL^{3A} construct, NorA-BRIL^{0A}, NorA-BRIL^{1A}, and NorA-BRIL^{2A} displayed BAG2 closer to NorA. For example, BAG2 in NorA-BRIL^{0A}

https://doi.org/10.1038/s41467-024-54986-5

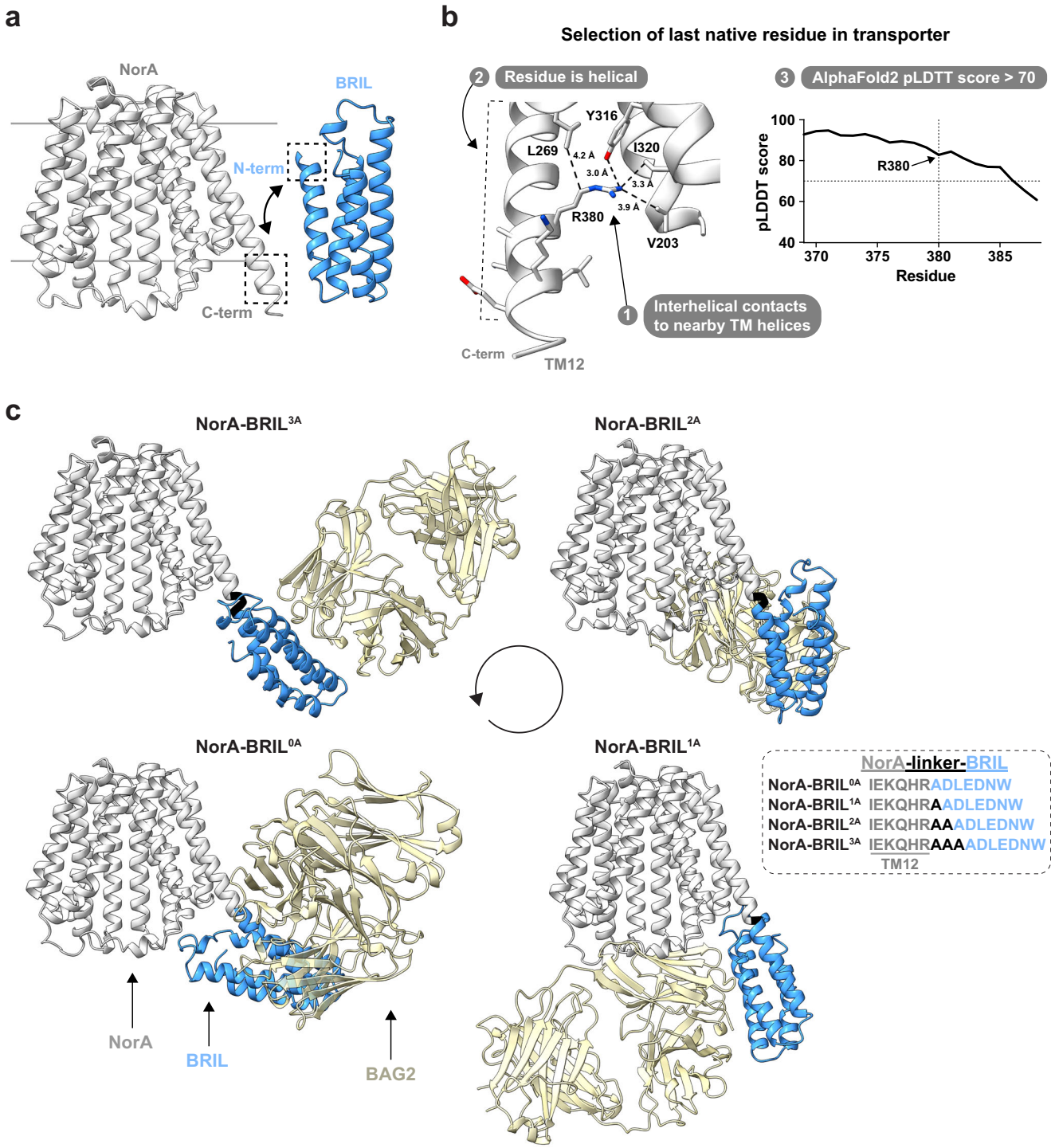

Fig. 1 | Design and prediction of NorA-BRIL structures. a Schematic representation of the shared helix approach where the C-terminal helix of NorA (gray) is adjoined to the N-terminal helix of BRIL (blue), as indicated with dashed boxes. **b** Three recommended criteria to select the last native residue to retain in the transporter's sequence. For NorA, Arg380 was selected since it was the last residue in the TM12 helix to satisfy the three criteria. **c** Fusion protein sequences and prediction of NorA-BRIL-BAG2 structural models. Left: The NorA-BRIL portion of the complexes (NorA in gray; BRIL in blue) were predicted using AlphaFold2, while BAG2 (pale yellow) was modeled by aligning BRIL from the crystal structure of BRIL-BAG2 (PDB ID: 6CBV)[34] with BRIL in the NorA-BRIL AlphaFold2 predictions. The counterclockwise arrow, starting from the lower left panel, indicates increasingly longer alanine linkers (black) from zero to three residues. Right: The dotted rectangle displays sequences of the four NorA-BRIL fusion proteins displaying a portion of TM12 of NorA (gray), the alanine residues of the linker (black), and the first helix of BRIL (blue).

and NorA-BRIL^{2A} were proximal to NorA, while NorA-BRIL^{1A} displayed the most overlap with BAG2. Nevertheless, to gauge the accuracy of predicted models, we initiated experiments on both NorA-BRIL^{1A} and NorA-BRIL^{3A}, which offered the greatest contrast in the predicted orientations of BAG2 relative to NorA.

Cryo-EM screening of NorA-BRIL constructs

We first attempted cryo-EM experiments on the NorA-BRIL^{1A} and NorA-BRIL^{3A} constructs without the help of any Fab. Cryo-EM samples were prepared for these fusion proteins in the absence of BAG2 by using the most concentrated fractions obtained from size-exclusion

chromatography (SEC) (Supplementary Fig. 1a, b). Following cryo-EM data collection and processing, 2D classes were obtained (Supplementary Fig. 1c, d). While some 2D classes in top views (perpendicular in the membrane region) showed helical features, we were unable to observe BRIL in 2D classes in side views for either sample, similar to a prior report[34]. These observations indicated that either the poly-alanine linker was flexible or the BRIL domain alone was insufficient for allowing 3D reconstruction of NorA.

To assess the linker's rigidity, a requirement for testing the validity of our approach, we performed binding assays of NorA-BRIL constructs to BAG2. SEC experiments revealed BAG2 induced left-shifted peaks upon binding NorA-BRIL^{1A} and NorA-BRIL^{3A}, and the NorA-BRIL^{3A}-BAG2 complex exhibited a greater peak intensity compared to NorA-BRIL^{1A}-BAG2 (Fig. 2a, b). The latter observation suggested the NorA-BRIL^{3A}-BAG2 complex was more stable, which likely stemmed from reduced steric interference (Fig. 1c).

Next, we collected and processed cryo-EM datasets for NorA-BRIL^{1A}-BAG2 and NorA-BRIL^{3A}-BAG2 complexes. Note that the NorA-BRIL^{1A}-BAG2 sample also contained Fab36, a NorA-specific outward-open binder[18]; however, since few NorA-BRIL^{1A} particles bound both BAG2 and Fab36, we only considered particles corresponding to NorA-BRIL^{1A}-BAG2 complexes (see Methods section "*Cryo-EM sample preparation and screening*"). The resulting 2D classes displayed the canonical two-lobe Fab structure and continuous density extending from BAG2 to NorA (Fig. 2c, d). Overall, these classes positioned BAG2 proximal to NorA in the NorA-BRIL^{1A} construct and distal to NorA in the NorA-BRIL^{3A} construct, in qualitative agreement with the predicted models (Fig. 1c). However, the 3D cryo-EM map for NorA-BRIL^{1A}-BAG2 deviated from the predicted model, showing NorA displaced by at least 20 Å from the corresponding density (Fig. 2e). This divergence likely stemmed from steric clash between BAG2 and NorA and was consistent with the lower purification yield of the complex from SEC experiments (Fig. 2a). In contrast, the cryo-EM map of the NorA-BRIL^{3A}-BAG2 complex revealed a striking similarity to the overall shape of the prediction, where BAG2 was positioned away from NorA and avoided steric clash (Fig. 2f). While the resolution in this small dataset was insufficient for deriving conclusions about NorA's conformation, these findings validated our design strategy of using AlphaFold2 to control the orientation of BRIL and BAG2 relative to NorA by using a short poly-alanine linker. Since the NorA-BRIL^{3A}-BAG2 complex was less likely to interfere with NorA's structure, this construct was determined to be suitable for cryo-EM studies.

Finally, an important consideration was whether the C-terminal truncation of NorA and fusion with BRIL influenced its function as an efflux transporter from *S. aureus*. To test this, we performed growth inhibition assays against norfloxacin, an antibiotic which NorA effluxes. NorA-BRIL^{3A} displayed a strong phenotype relative to a dead mutant NorA control and was similar to wild-type NorA (Supplementary Fig. 1e, f). These functional results support the conclusion that the NorA-BRIL^{3A} fusion protein is minimally invasive to NorA's structure and activity.

Multiple conformations of NorA resolved from a single cryo-EM sample

Using NorA-BRIL^{3A} bound to BAG2, we set out to test whether a high-resolution cryo-EM map could be obtained using this fusion protein construct. We reasoned a sample at pH 5.0 would be suitable for the experiment since our team recently discovered NorA populates an inward-occluded structure when two membrane embedded residues Glu222 and Asp307 were protonated[18]. While this structure required the use of a NorA specific antibody (FabDA1) to capture the inward-occluded state, we envisioned this conformation could be observed in the "wild-type" fusion protein at low pH to facilitate the protonation of the above-mentioned acidic residues in the absence of the antibody. Cryo-EM experiments with NorA-BRIL^{3A} at pH 5.0 would test the suitability of the fusion strategy to solve atomic resolution structures without a NorA-specific antibody. To this end, we prepared a cryo-EM sample of the NorA-BRIL^{3A}-BAG2 complex at pH 5.0 (Supplementary Fig. 1g, h).

Following collection of a large cryo-EM dataset and processing without masking, we obtained three uniform cryo-EM maps corresponding to NorA in the inward-open, inward-occluded, and occluded conformations (Supplementary Fig. 2; Supplementary Fig. 3a–c). Notably, the linker adjoining NorA and BRIL displayed continuous density in all three maps, suggesting rigidity between BAG2 and NorA. In each map, the linker connecting NorA and BRIL displayed a local resolution of ~3.3 Å (Supplementary Fig. 3a–c). Alternative processing of the same dataset into a single ab initio 3D class resulted in a 2.86 Å cryo-EM map with densities partially missing in the N-terminal domain of NorA (TM1 to TM6) relative to the C-terminal domain (TM7 to TM12) (Supplementary Fig. 3d). Adding up the particle numbers across the three isotropic maps (Supplementary Fig. 3a–c) roughly equated to the particle number in this anisotropic map (Supplementary Fig. 3d), suggesting the missing density of the N-terminal domain likely stemmed from the presence of multiple conformations. In each case, the local resolution of the NorA-BRIL^{3A} linker, regardless of the processing, mirrored the overall map resolution: 2.8 Å local resolution of the linker for the anisotropic map and 3.3 Å local resolutions for the three isotropic maps. This observation suggested that the linker rigidity extended to NorA and directly assisted particle alignment, thereby improving the overall resolution of the entire construct. This improvement enabled residues within the substrate binding pocket to display local resolutions near the overall map resolution.

The final cryo-EM processing step involved masking around NorA to enhance the quality of the N-terminal domain for the three isotropic maps, leading to final map resolutions spanning from 3.18 to 3.25 Å (Fig. 3a; Supplementary Fig. 2; Supplementary Fig. 4; Supplementary Table 1). These resolutions compared favorably to the NorA-FabDA1 cryo-EM map at 3.26 Å resolution, where FabDA1 stabilized an inward-facing state of NorA[54]. The quality of the three maps afforded unambiguous modeling of the backbone and side chains of NorA TM domain helices and the linker to the BRIL domain (Fig. 3b; Supplementary Fig. 5). Cross-sections of the three structures revealed differential accessibility of the substrate binding pocket from the cytoplasmic side of the membrane, consistent with inward-open, inward-occluded, and occluded classifications (Fig. 3c). Notably, the inward-open structure was in best agreement with the AlphaFold2 predicted model in Fig. 1c by displaying a 0.704 Å r.m.s.d (Supplementary Fig. 6a). Superimposition of NorA in the inward-occluded and occluded structures with NorA in the inward-occluded state in complex with FabDA1[54] revealed backbone r.m.s.d. values of 1.076 Å and 1.373 Å (Supplementary Fig. 6b, c). The greater similarity of the former structures and the accessibility of the substrate binding pocket supported the characterization of these conformations. Although the NorA-BRIL^{3A} fusion construct was designed based on the inward-open conformation of the protein, the simultaneous observation of two additional conformations from the same sample shows a great advantage of our approach. The presence of three conformations within the ensemble at pH 5.0 indicated that FabDA1 likely bound to NorA through a conformational selection mechanism since the inward-occluded structure most closely resembled NorA's conformation when in complex with FabDA1. These results also emphasize the flexible nature of NorA's structure and the power of synthetic antibodies to stabilize specific conformations. The successful demonstration that our strategy is compatible with deciphering multiple conformations of the transporter is complementary to biophysical techniques such as NMR spectroscopy and single-molecule FRET for quantifying structural dynamics and conformer populations within ion-coupled transport cycles[59–62]. Note that

https://doi.org/10.1038/s41467-024-54986-5

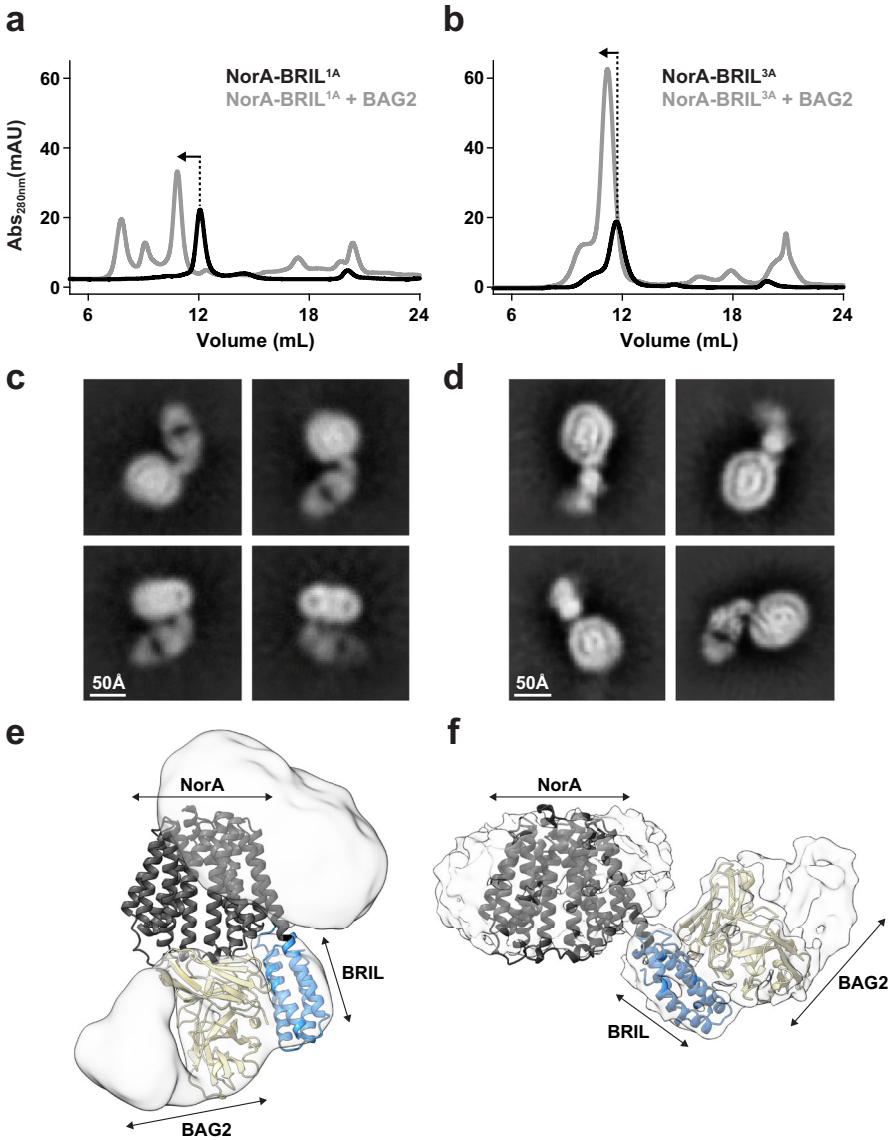

Fig. 2 | Binding experiments and cryo-EM of NorA-BRIL^{1A} and NorA-BRIL^{3A} in complex with BAG2. a, **b** SEC chromatograms of NorA-BRIL^{1A} (**a**) and NorA-BRIL^{3A} (**b**) in PMAL-C8 at pH 7.5 in the absence (black traces) or presence of three-fold excess BAG2 (gray traces). Arrows indicate the SEC peaks corresponding to NorA-BRIL alone or NorA-BRIL-BAG2 complexes. In each experiment, the same amount of NorA-BRIL was injected. For NorA-BRIL^{1A}, the peak displayed a 1.41-fold increase in the peak integration after BAG2 addition. For NorA-BRIL^{3A}, the peak displayed a 3-fold increase in the peak integration after BAG2 addition. **c**, **d** Exemplary 2D classes of NorA-BRIL^{1A}-BAG2 (**c**) and NorA-BRIL^{3A}-BAG2 complexes (**d**). The total number of particles were 11,127 and 11,053 for **c**, **d**, respectively. **e**, **f** Superimposition of cryo-EM maps of NorA-BRIL^{1A}-BAG2 (**e**) and NorA-BRIL^{3A}-BAG2 complexes (**f**) displayed in partially transparent gray surface and the corresponding predicted model shown in cartoon (NorA in dark gray; BRIL in blue; BAG2 in pale yellow; linker in black). Only the F_v portion of BAG2 is displayed. In each panel, BRIL and the F_v portion of BAG2 of the model were aligned to the respective cryo-EM map using Chimera[95]. The different parts of the model are named and indicated using double sided arrows. Due to the resolution, the superimposition is used to assess the relative agreement of NorA-BRIL relative to BAG2 and not to assign NorA's conformation (i.e., inward- or outward-facing).

additional discussion of the structures is provided in the Supplementary Information along with detailed structural views in Supplementary Fig. 7.

Cryo-EM structure of outward-facing NorA

To complement the inward-facing and occluded structures of NorA at pH 5.0 and further benchmark the approach, we sought to determine an outward-facing conformation of NorA at pH 7.5 using the same NorA-BRIL^{3A} fusion construct. We previously showed that the antibody Fab36 bound NorA from the extracellular side of the membrane by inserting its CDRH3 loop into the substrate binding pocket of NorA, yielding an outward-open conformation[18]. A cryo-EM sample of NorA-BRIL^{3A} in complex with both BAG2 and Fab36 at pH 7.5 was prepared and used to collect a large cryo-EM dataset (Supplementary Fig. 8a, b). Following data processing, we obtained a cryo-EM map of this complex containing two Fabs at 2.56 Å resolution (Supplementary Fig. 8c; Supplementary Fig. 9; Supplementary Table 1). While the 2D classes displayed clear density corresponding to BRIL and BAG2 (Fig. 4a), the density for BRIL and a portion of BAG2 was very weak in the final cryo-EM map (Fig. 4b, c). This likely occurred because NorA-Fab36 served as the gravity center of the entire complex due to the extensive interactions made between CDRH3 of Fab36 and the substrate binding pocket of NorA. Nevertheless, we hypothesized that BRIL/BAG2 retained its ability to serve as a fiducial mark even though its density was weaker in the cryo-EM map. Two observations supported this conclusion and underscored that the linker between NorA and BRIL remained rigid.

https://doi.org/10.1038/s41467-024-54986-5

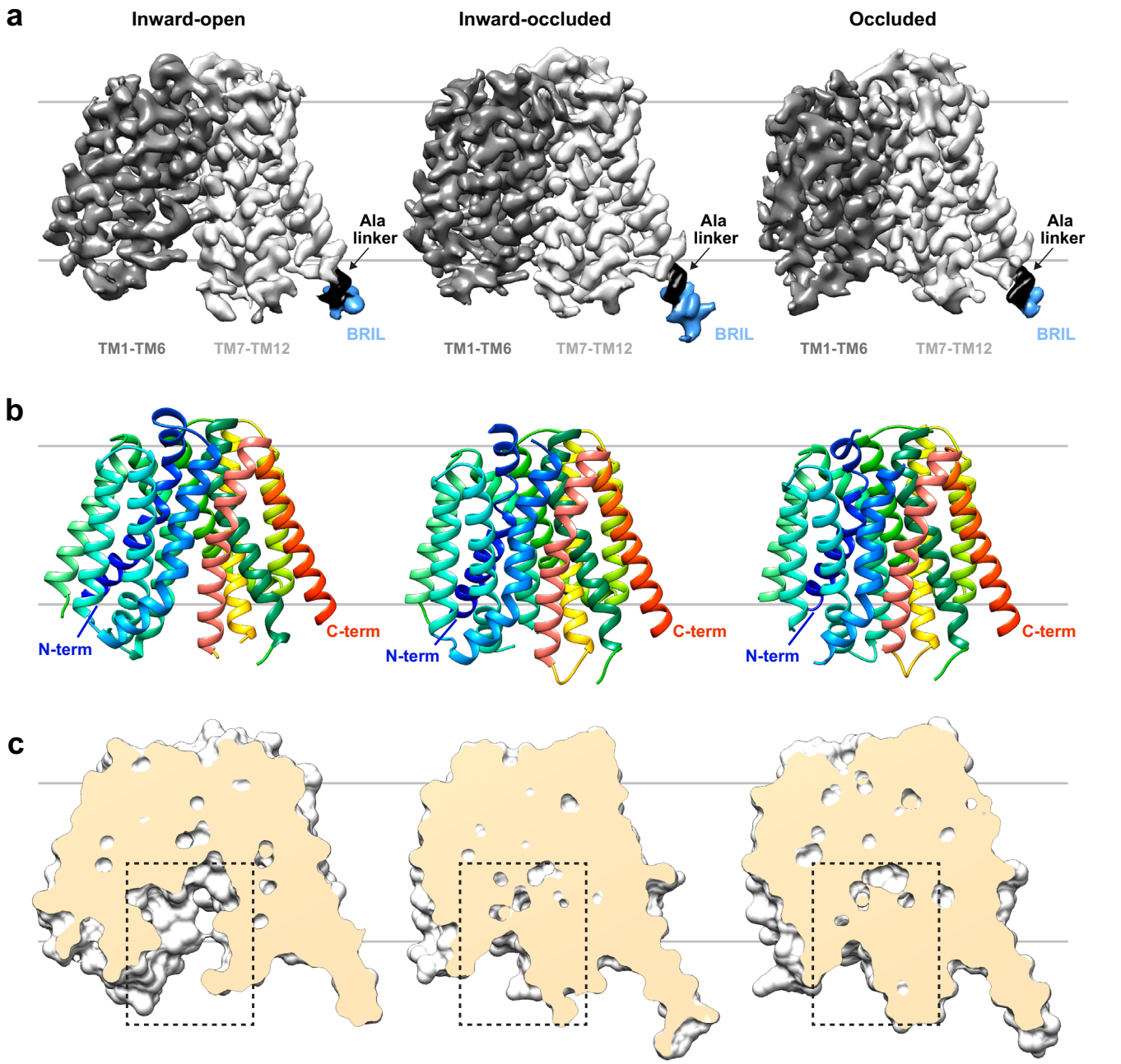

Fig. 3 | Cryo-EM maps and structures of masked NorA-BRIL^{3A} at pH 5. a Cryo-EM maps of masked NorA-BRIL^{3A} at pH 5.0 in inward-open (left), inward-occluded (middle), and occluded conformations (right), with map resolutions of 3.21 Å, 3.18 Å, and 3.25 Å, respectively. Maps are colored by the N-terminal domain of NorA (TM1 to TM6; in dark gray), C-terminal domain of NorA (TM7 to TM12; in light gray), alanine linker (in black), and BRIL (in blue). **b** Structures of NorA in the inward-open (left), inward-occluded (middle), and occluded (right) conformations, where NorA is displayed in a cartoon representation (TM helices in rainbow). Side views are depicted in the same orientation as the maps. **c** Cross-sections of NorA in the inward-open (left), inward-occluded (middle), and occluded (right) conformations, where NorA is displayed in a surface representation and the substrate binding pocket is indicated in the boxed region (same box size for all).

First, the three alanine residue linker and a portion of the first helix of BRIL displayed local resolutions of ~2.8 Å, which were near the overall map resolution (Fig. 4d). Second, the overall map resolution was markedly higher for the NorA-BRIL^{3A}-Fab36 portion of the fusion complex (2.56 Å) relative to our published NorA-Fab36 cryo-EM map (3.16 Å)[18] (Supplementary Fig. 9d). While the two maps exhibited a strong similarity, the cryo-EM map from the fusion construct displayed more well-defined densities (Fig. 5a, b). This result indicated that the BRIL fusion approach worked synergistically with an existing target-specific Fab to enhance the resolution, a finding that may be applicable for improving the resolution of other MFS transporters. From this map, all 12 TM helices of NorA and the Fab36 CDRH3 loop that inserted into NorA's substrate binding pocket were precisely modeled (Supplementary Fig. 10).

The refined model aligned closely with the outward-open structure of NorA in complex with Fab36 (PDB ID: 7LO8), displaying an r.m.s.d. of 1.047 Å (Fig. 5c). The higher overall resolution of the new structure likely accounts for the r.m.s.d. difference. Indeed, residues within and surrounding CDRH3 showed local resolutions of ~2.3 Å (Fig. 5d). As expected from the improved resolution, intermolecular distances within the NorA-Fab36 complex were more clearly defined with a few key interactions between the CDRH3 loop and NorA residues differing up to 0.6 Å relative to our prior report. Nevertheless, all contacts previously reported remained intact and the overall

https://doi.org/10.1038/s41467-024-54986-5

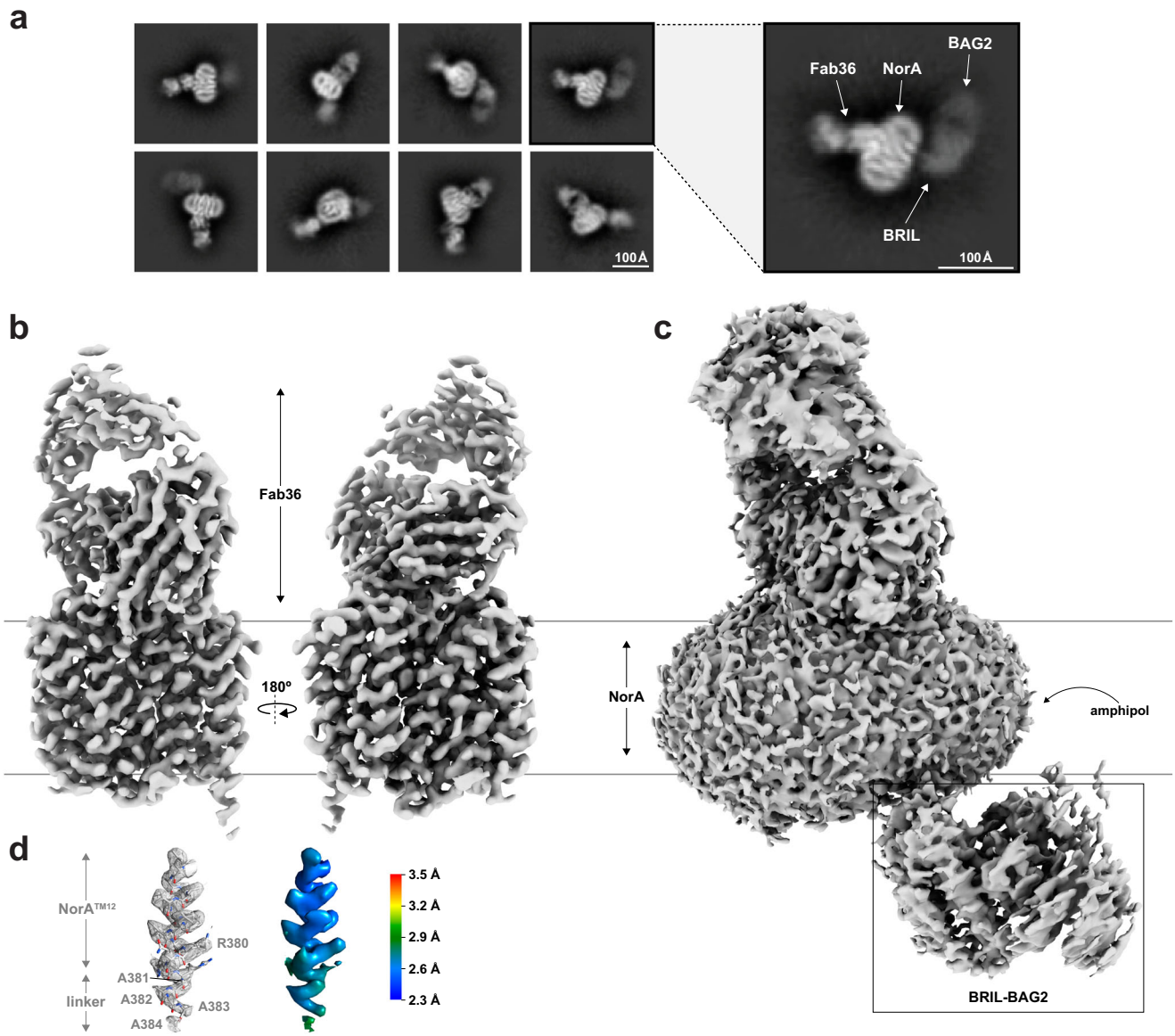

Fig. 4 | Cryo-EM results of the NorA-BRIL^{3A}-BAG2-Fab36 sample. a Exemplary cryo-EM 2D classes of the NorA-BRIL^{3A}-BAG2-Fab36 sample at pH 7.5. The expanded view on the right displays one of the 2D classes, denoting regions within the complex corresponding to NorA, BRIL, BAG2, and Fab36. **b** Two views of the cryo-EM map of the NorA-BRIL^{3A}-BAG2-Fab36 sample displayed at 10σ, where σ is the standard deviation of the map. Parallel gray lines indicate a representation of the lipid bilayer containing NorA. **c** Cryo-EM map of the NorA-BRIL^{3A}-BAG2-Fab36 sample displayed at 3σ. The boxed region corresponds to the BRIL and BAG2 domains. **d** Model-to-map superimposition (left) and local resolution cryo-EM map (right) for a portion of TM12 of NorA and the alanine linker connecting NorA and BRIL for the NorA-BRIL^{3A}-BAG2-Fab36 sample. The cryo-EM map is displayed in gray mesh and the model is shown in a stick representation (gray for carbon, red for oxygen, blue for nitrogen). For the local resolution map, higher resolution is depicted in blue and lower resolution is shown in red.

interaction surface was unchanged. Taken together with our inward-open, inward-occluded, and occluded structures determined in the NorA-BRIL^{3A} sample at pH 5.0, this outward-open structure paves the way for additional mechanistic studies, including structures of NorA bound to substrates and inhibitors. The latter will serve to guide improvements to inhibitor potency and specificity that would otherwise be difficult to accomplish in the absence of the described fusion protein approach.

Applicability of method to other MFS transporters

The application of the BRIL fusion strategy to NorA suggested this approach may apply more broadly to other MFS transporters tolerating truncation of the C-terminus. To quantitatively estimate this fraction of MFS transporters, we analyzed 1,118 proteins contained within 103 MFS subfamilies from the Transporter Classification Database[63], representing proteins from all domains of life. Our findings indicate that most MFS transporters possessed <20 residues after the last residue in the terminal TM helix (Fig. 6a). Structural inspection of these proteins using AlphaFold2 revealed that 50% were predicted to contain disordered C-termini, as characterized by "low confidence" pLDDT scores (i.e., pLDDT scores between 50 and 70) (Fig. 6b, c). Another 25% were predicted to contain mostly disordered C-termini but displayed a few residues with pLDDT values above 70 (Fig. 6d, e). The final 25% of predicted structures displayed several C-terminal residues with pLDDT values above 70, indicative of more extensive structure (Fig. 6f, g). Proteins in this category and structurally similar ones are unlikely to be applicable to the method. Based on this analysis, we estimate that C-terminal extension of MFS transporters to the BRIL domain is

https://doi.org/10.1038/s41467-024-54986-5

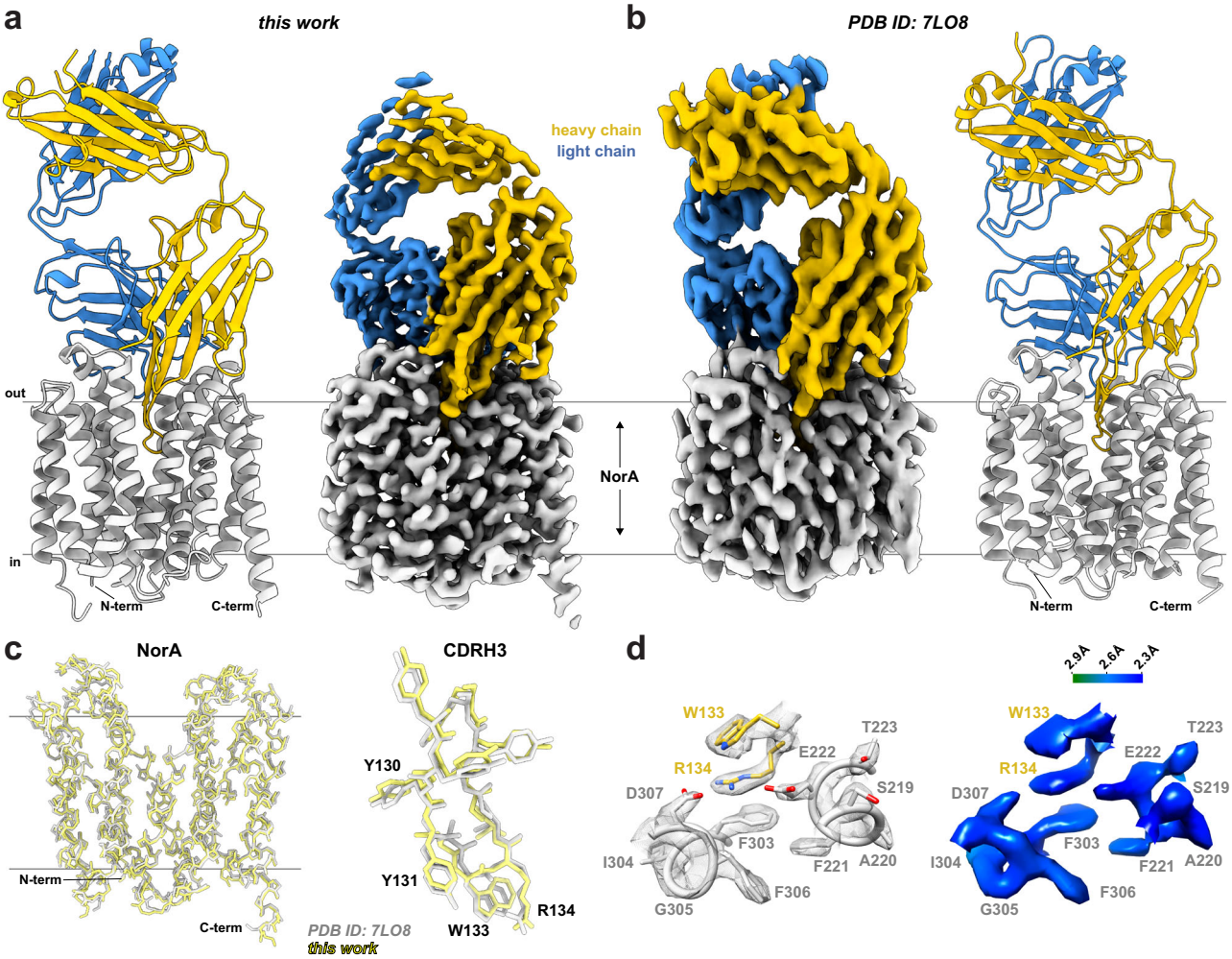

Fig. 5 | Resolution of the outward-open cryo-EM structure of NorA is improved using the BRIL fusion approach. a Structure (left) and cryo-EM map (right) of the NorA-BRIL^{3A}-BAG2-Fab36 sample displaying NorA (gray) and Fab36 (heavy chain in light orange, light chain in blue). The overall cryo-EM map resolution is 2.56 Å. The cryo-EM map is displayed at 10σ, where σ is the standard deviation of the map. **b** Published structure (right) and cryo-EM map (left) of the NorA-Fab36 complex displaying NorA (gray) and Fab36 (heavy chain in light orange, light chain in blue)[18]. The overall cryo-EM map resolution is 3.16 Å. The cryo-EM map is displayed at 10σ. **c** Superimpositions of NorA (left) and CDRH3 (right) for structures of NorA-BRIL^{3A}-Fab36 (pale yellow) and NorA-Fab36 (PDB ID: 7LO8, gray). The backbone r.m.s.d. values for NorA and CDRH3 are 0.626 Å and 0.554 Å, respectively. **d** Model-to-map fit (left) and local resolution cryo-EM map (right) displaying select regions around the CDRH3 loop that inserts into the NorA substrate binding pocket. The cryo-EM map is displayed in gray mesh and the model is shown in a stick representation (gray for carbons of NorA, pale yellow for carbons of CDRH3, red for oxygen, blue for nitrogen). For the local resolution map, higher resolution is depicted in blue and lower resolution is shown in green.

applicable to ~50–75% of proteins within this family. Further dissection by MFS subfamily revealed that some subfamilies displayed higher or lower propensities relative to this range which is expected given structural conservation within the groups (Fig. 6h; Supplementary Table 2).

Next, we aimed to design MFS-BRIL fusion proteins for transporters without significantly ordered structure on the C-terminus (i.e., from Fig. 6b, d). A summary of the overall workflow is provided in Supplementary Fig. 11. We selected 20 MFS transporters from different subfamilies, including 10 from bacteria and 10 from eukaryotes (Supplementary Table 3). The selection criteria summarized in Fig. 1b were implemented starting from AlphaFold2 models, where the last native residue of the target transporter possessed a helical secondary structure, displayed interhelical contacts to other TM domains, and showed an AlphaFold2 pLDDT confidence score >70 (Supplementary Fig. 12a, b; Supplementary Table 3). For each protein, AlphaFold2 was then used to predict fusion protein structures using linkers ranging from zero to eight alanine residues. Following AlphaFold2 predictions, the most suitable fusion protein sequences were selected after analyzing for clashes with BRIL and BAG2 and considering pLDDT confidence scores of the fusion protein (Supplementary Fig. 12b; Supplementary Table 3). For the pLDDT values, greater confidence scores have been correlated to increased rigidity[64] and we therefore used this as a guide to select among fusion proteins that provided clash-free predictions. Notably, we found about half of the constructs achieved approximately the same pLDDT scores between wild-type and the fusion protein when comparing native residues, while the other half displayed somewhat lower pLDDT scores than the wild-type. The NorA-BRIL^{3A} construct clustered into the latter half, suggesting that slightly lower values still confer rigidity. However, for almost every fusion protein, we found that the linker and start of the BRIL domain showed overall higher confidence scores relative to the native C-terminal residues (Supplementary Fig. 12b). The length of alanine linker varied among the optimal fusion constructs since the last native residue of the transporter was not always in the same registry of the terminal TM helix (Supplementary Fig. 12a). For example, some fusion proteins (e.g., Bmr-BRIL^{7A} and Blt-BRIL^{7A}) required a linker length up to seven alanine residues to avoid steric clash and preserve a continuous

https://doi.org/10.1038/s41467-024-54986-5

helix between the transporter and BRIL (Supplementary Fig. 12c). In contrast, other transporters required a short linker or no additional alanine residues, such as GlpT, to yield a suitable fusion construct.

To experimentally test the designs, we selected GlpT, Bmr, and Blt as a subset from two of the most populous subfamilies of MFS transporters (2.A.1.2 and 2.A.1.4). GlpT is a glycogen phosphate transporter from *E. coli*[58], while Bmr and Blt are *B. subtilis* transporters involved in multidrug resistance[65,66]. Constructs were first purified and tested for binding to BAG2. For each system, we observed the complex of the fusion protein and BAG2 shifted to the left by ~1 mL in SEC chromatograms, similar to that observed for NorA-BRIL binding to BAG2 (Fig. 7a–c; Supplementary Fig. 13). Next, we collected small cryo-EM datasets of each complex to gauge the quality of the images and rigidity of the constructs. 2D class averages for each sample displayed

Fig. 6 | Statistical analysis of MFS proteins to gauge applicability of the BRIL fusion strategy to MFS transporters. a Histogram plot of the length of the C-terminal tail following the terminal TM helical residue in the structure of 1,118 MFS proteins. Note that 54 proteins displayed tail lengths >120 residues and are not shown. **b**, **d**, **f** AlphaFold2 pLDDT values plotted as a function of residues following the terminal TM helix for a total of 100 MFS structures. The residue after the terminal TM helix was renumbered as residue 1. Using this nomenclature, proteins with no pLDDT values above 70 after residue 4 clustered into the 50% category displayed in (**b**). Proteins with pLDDT values above 70 for residues 5 −14 clustered into the 25% category displayed in (**d**). Proteins with pLDDT values above 70 for residues 15 and beyond clustered into the 25% category displayed in (**f**). The dotted line indicates the pLDDT value of 70, which is the "confident" cutoff used in AlphaFold2. **c**, **e**, **g** Example AlphaFold2 predicted structures for each of the categories in **b**, **d**, and **f**. Each protein is indicated by the Uniprot ID. All residues up to and including the terminal TM helix are colored in gray. Residues with pLDDT values above 70 are colored in blue and those below 70 are colored in magenta, as indicated in the schematic above (**c**). In each predicted structure, TM12 and the C-terminus is indicated. **h** Plot of the estimated applicability of the BRIL method presented in this work as a function of different MFS subfamilies. Bars display the percentage of proteins within each subfamily with no pLDDT values above 70 after residue 4 (like those in **b**). The error bars represent the upper limit percentage of proteins with pLDDT values above 70 only for residues 5 to 14 (like those in (**d**)). A complete list of MFS subfamilies and applicability is displayed in Supplementary Table 2.

the transporter, BRIL, and BAG2 in the designed conformation, where BAG2 was extended away from the transporter as in the NorA fusion protein (Fig. 7d–f; Supplementary Fig. 12c). Likewise, 3D reconstructions showed continuous density connecting the transporter and BRIL, supporting a rigid linker and with the cryo-EM density overlapping with the predicted structure of the complex (Fig. 7g–i). The quality of these cryo-EM data was comparable to screening datasets of NorA-BRIL^{3A} (i.e., compare with Fig. 2e, f), indicating the feasibility of using our strategy more broadly for structure determination of MFS transporters. Taken together with cryo-EM-derived structures of NorA-BRIL^{3A} bound to BAG2, we conclude that the strategy to fuse BRIL with the C-terminal end of MFS transporters will be a beneficial tool for studying this family of proteins.

Discussion

In this work, we described a strategy for designing a rigid MFS transporter-BRIL fusion protein and validated it using four transporters from this family with cryo-EM. Notably, the method allowed for multiple cryo-EM structures to be determined for NorA, a 42 kDa MFS transporter near the theoretical minimum for cryo-EM structure determination. By introducing a short poly-alanine linker between NorA and BRIL, we obtained a linker resolution of ~2.8 to 3.3 Å that propagated to the substrate binding pocket of NorA. It is likely that the rigid linker facilitated these conformations to be deciphered during cryo-EM data processing, leading to three structures elucidated from a single sample. A key to this design was identification and removal of flexible residues from the C-terminus of the transporter and selection of the linker length to adjust BRIL's orientation to avoid clashes and increase the effectiveness of particle alignment. The design workflow is described in Supplementary Fig. 11 in a step-by-step format.

From our analysis in Fig. 6, we estimated C-terminal fusion of BRIL to MFS transporters is relevant for ~50–75% of proteins within the family. MFS transporters comprise the largest family of secondary active transporters in nature and display a broad range of biological functions and substrate specificities, including transport of ions, metabolites, peptides, and drugs[49–51]. For example, MFS multidrug efflux transporters such as NorA and MdfA are involved in antibiotic efflux by binding and transporting a variety of structurally distinct molecules[67,68], while other transporters involved in metabolism and growth such as GlpT and GLUT4 display a narrower range of substrate specificity[69,70]. Since there are no systematic design strategies to solve cryo-EM structures of small MFS transporters, we envision our approach of fusing a compact four-helix bundle to a TM helix distant from the substrate binding pocket will facilitate determination of substrate bound structures and offer a tool to interrogate intermolecular interactions underlying substrate specificity.

Creation of fusion proteins in the literature differ in the flexibility of the linker between the fiducial mark and the target protein and the location of the fusion partner in a loop or at a terminus[24,27,71,72]. Flexible linkers are more likely to retain correct protein folding at a cost of resolution due to poorer particle alignment. A successful example of this approach involved fusion of BRIL to the folate transporter SLC19A1 using the transporter's native, unstructured N-terminus[38]. The cryo-EM structure revealed BRIL positioned parallel to the TM domains of the transporter and stabilized by electrostatic interactions with a loop from SLC19A1. Since BRIL was fortuitously stabilized by interactions with the transporter's loop residues, this strategy is unlikely to be translatable to other MFS transporters. An alternative strategy is to introduce a rigid linker to the fiducial mark by extending a TM helix (i.e., the "shared helix" approach[34,47]), enabled by the fact that most transporters contain TM helices. Elegant examples of this idea have been introduced by incorporating BRIL at the N-terminus of the potassium channel KcsA[34] and fusing short epitope sequences to the termini of small membrane proteins[73,74]. The former utilized poly-alanine linkers and others incorporating Arg, Lys, Phe, and Glu residues to demonstrate topological control of BRIL and BAG2. Similarly, the short epitope sequence can be efficiently incorporated into the target protein sequence and recognized by antibodies. Nevertheless, prior to this work, there have been limited successful applications in deriving atomic resolution cryo-EM maps or structural models upon fusion to small membrane protein transporters. Furthermore, our work proposes three quantitative criteria for identifying the last terminal residue to retain within the native transporter (Fig. 2b; Supplementary Fig. 11) and shows that selection of a short and optimal poly-alanine linker facilitates determination of atomic resolution structures, including three NorA structures from a single cryo-EM sample. It is likely that a structured linker coupled with recognition of the tertiary structure of BRIL by BAG2 conferred rigidity between the transporter and Fab, ultimately providing improved particle alignment in cryo-EM data processing relative to recognition of a single helical domain as in the epitope fusion strategy. Regarding the BRIL-KcsA fusion protein, this is a difficult model system since KcsA forms a tetramer and each monomer contains only two TM helices.

Prior to our findings, it has been unclear whether a single rigid fusion of a fiducial mark to a small membrane protein is sufficient for structure determination by cryo-EM. In fact, there are more successful examples of cryo-EM structures derived from double tethering BRIL and other fiducial marks into loops adjoining TM helices. One study investigated the adenosine A2a receptor-BRIL construct used for X-ray crystallography[28] and resolved a cryo-EM structure in complex with BAG2[23]. The cryo-EM map displayed two continuous helices adjoining BRIL to the receptor by using only the native residues of the receptor. However, when the authors engineered one continuous helix and one flexible linker to BRIL, the map quality did not afford structure determination. Other cryo-EM structures for different GPCRs have also been elucidated by grafting the linker residues from the adenosine A2a receptor onto the target receptor (i.e., ARRQL from A2a to the N-terminus of BRIL and ERARSTL from A2a to the C-terminus of BRIL)[39–42]. Furthermore, the adenosine A2a receptor linker was used to fuse BRIL between TM8 and TM9 of the MFS transporter VMAT2, which resulted in a structure of a dimer where the authors noted the potential of an artifact induced by the BRIL fusion[37]. Lastly, unlike the work on the adenosine A2a receptor, a similar BRIL fusion junction

https://doi.org/10.1038/s41467-024-54986-5

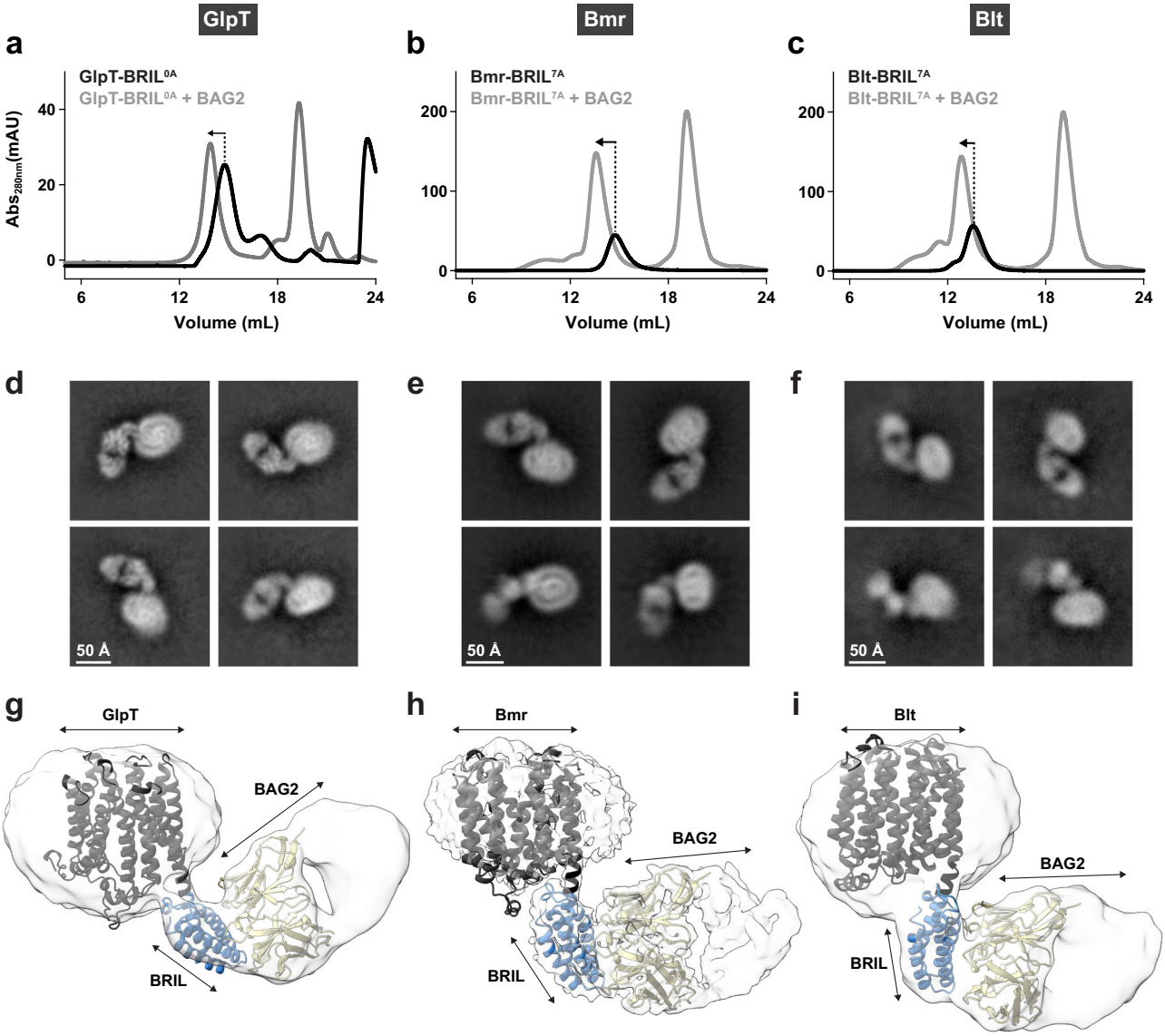

Fig. 7 | Application of helical fusion approach to three additional MFS transporters. a–c SEC chromatograms of GlpT-BRIL^{0A} (**a**), Bmr-BRIL^{7A} (**b**), and Blt-BRIL^{7A} (**c**) in PMAL-C8 in the absence (black traces) or presence of three-fold excess BAG2 (gray traces). Arrows indicate the SEC peak shifts of the MFS-BRIL fusion proteins upon BAG2 binding. **d–f** Exemplary 2D classes of GlpT-BRIL^{0A}-BAG2 (**d**), Bmr-BRIL^{7A}-BAG2 (**e**) and Blt-BRIL^{7A}-BAG2 (**f**) complexes. **g–i** Superimposition of cryo-EM maps of GlpT-BRIL^{0A}-BAG2 (**g**), Bmr-BRIL^{7A}-BAG2 (**h**), and Blt-BRIL^{7A}-BAG2 (**i**) complexes displayed in partially transparent gray surface and the corresponding predicted model shown in cartoon (GlpT, Bmr, and Blt in dark gray; BRIL in blue; BAG2 in pale yellow; linker in black). Only the F_v portion of BAG2 is displayed. In each panel, BRIL and the F_v portion of BAG2 of the model were aligned to the respective cryo-EM map using Chimera[95]. The different parts of the model are named and indicated using double sided arrows. The total number of particles were 12,164, 66,568, and 10,857 for (**g–i**) respectively.

applied to the β2-adrenergic receptor was unsuccessful for structure determination in the absence of a bivalent nanobody further rigidifying the construct[22]. In contrast to these reports indicating that multiple tethering contacts of the fiducial mark are required for cryo-EM structure determination, our findings show that a single rigid linker between the terminal TM helix of an MFS transporter and BRIL is sufficient. A graphical summary of the above discussion is provided in Supplementary Fig. 14.

An alternate approach to rigid linkers is the incorporation of split N- and C-terminal binding partners fused to the target protein with flexible linkers such that their interaction creates a fiducial mark[46,75,76]. The drawback of this approach, in contrast to a single fusion like the one used in this work, is the requirement to manipulate both the N- and C-termini of the target protein and the need to screen multiple samples since the split fusion pair is not rigidly coupled to the termini of the target.

The final category of universal fiducial marks involves the development of Fabs or scaffolds that bind or are fused with small synthetic binding proteins that do not interfere with the target protein interface[14,77,78]. While this approach is a powerful technology for stabilizing higher energy conformations and increasing the overall size of the system for cryo-EM structure determination, the drawback is the need to identify a nanobody binder to the target protein.

Relative to the fiducial assisted strategies discussed above, the approach described in this work offers four advantages. First, design of the fusion construct is simple and modular in nature without the need for extensive protein engineering. Eliminating multiple tethers or cages to reinforce the interface of the fusion protein minimizes potential risks of perturbing the native structure of the protein while retaining the ability to resolve atomistic structures (~3 Å). Second, the orientation of BRIL and BAG2 can be predicted with AlphaFold2 and structural superimposition simply by changing the length of the

alanine linker. This reduces the time-consuming and costly step of screening constructs for cryo-EM and minimizes potential overlap of the fiducial marker and native binding surfaces within the target protein which may lead to folding problems. Third, the rigidity of the construct emerging from our strategy is compatible with resolving multiple conformations of the transporter in a single sample, if those conformations exist in the ensemble. Since secondary active transporters transition between different conformations, the successful implementation of this approach may expedite mechanistic studies for other MFS transporters. Fourth, the location of the BRIL fusion at a position of the transporter that does not play a major role in substrate binding or translocation may allow for structure determination of substrate-bound structures. Taken altogether, the strategy for creating a suitable fusion construct described in this work will be a valuable tool for resolving small MFS transporter structures in multiple conformations using cryo-EM, including those in complex with substrates, ligands, and inhibitors.

Methods

Fab expression and purification

The BAG2 gene[34], rigidified in the elbow region of the heavy chain[79], was purchased (Twist Bioscience), subcloned into a pTac expression vector, and transformed into the 55244 strain of *E. coli* (ATCC). BAG2 and Fab36 were expressed and purified with essentially the same procedure we previously reported[18]. *E. coli* harboring the Fab plasmids were expressed through leaky expression by incubation for 24 h at 30 °C in TBG media. Cells were harvested by centrifugation and stored at −80 °C. Cell pellets were resuspended and homogenized in running buffer (20 mM sodium phosphate pH 7.0) supplemented with 1 mg/mL hen egg lysozyme (Sigma). After centrifuging at 12,000 r.p.m. (17,418 x g, maximum) for 2 h at 4 °C in a Beckman centrifuge equipped with a JA-25.50 rotor (Beckman Coulter), the pellet was discarded and the supernatant loaded onto a protein G column (Cytiva) equilibrated in running buffer. Following washing steps using the running buffer to remove unwanted proteins, the targeted Fab was eluted with 100 mM glycine (pH 2.7) and neutralized with 2 M Tris buffer (pH 10). Peak fractions of purified Fab were combined and concentrated to 15 – 25 mg/mL using an Amicon ultra centrifugal filter with a 10 kDa nominal cutoff molecular weight (Millipore). Concentrated Fabs were flash-frozen and stored at −80 °C until complex assembly with the purified NorA-BRIL construct.

NorA-BRIL construct expression and purification

NorA-BRIL genes (NorA-BRIL^{1A} and NorA-BRIL^{3A}) were purchased harboring C-terminal decahistidine tags (Twist Bioscience) and subcloned into a pET29b vector. The vectors were transformed into C43 (DE3) *E. coli* and autoinduced with essentially the procedure previously reported[18]. Cells were grown with shaking at 32 °C in ZYP-5052 medium supplemented with 1 mM $MgSO_4$. The incubation temperature was reduced to 20 °C at an OD_{600nm} of 0.5-0.6 and incubated for 20–22 h. Cells were harvested by centrifugation and stored at −80 °C until further use.

Cell pellets were thawed, resuspended, and homogenized in lysis buffer (40 mM Tris pH 8.0, 400 mM NaCl, 10% glycerol), and centrifuged at 7,000 r.p.m. (5,927 x g, maximum) for 20 min at 4 °C in a Beckman centrifuge equipped with a JA-25.50 rotor (Beckman Coulter) to clarify the resulting lysate. For each construct, the membrane fraction was isolated by centrifuging for 2.5 h at 35,000 r.p.m. (142,688 x g, maximum) using a Beckman ultracentrifuge equipped with a Type 45 Ti fixed-angle rotor (Beckman Coulter). Subsequently, membrane fractions were solubilized in 20 mM Tris pH 8.0, 400 mM NaCl, 10% glycerol (v/v), 10 mM imidazole, and 1% (w/v) lauryl maltose neopentyl glycol (LMNG; Anatrace). Cobalt affinity resin (Thermo Fisher Scientific) was mixed with solubilized membrane fractions and incubated at 4 °C for 40 min to bind NorA-BRIL proteins. After washing away unwanted proteins with wash buffer (20 mM Tris pH 8.0, 400 mM NaCl, 10% glycerol (v/v), 0.2% (w/v) LMNG, 30 mM imidazole), NorA-BRIL protein was eluted with 400 mM imidazole. Subsequently, the carboxy-terminal decahistidine tag in the elution fractions was removed from NorA-BRIL by incubation with tobacco etch virus (TEV) protease at 4 °C for 8 – 12 h and subsequently dialyzed into SEC buffer (20 mM Tris pH 7.5 and 400 mM NaCl). The mixture for each construct was passed over the cobalt affinity column to separate NorA-BRIL^{1A} and NorA-BRIL^{3A} present in the flow through from TEV captured in the affinity resin. NorA-BRIL fractions were incubated with PMAL-C8 amphipol (Anatrace) at a final concentration of 0.06% (w/v) for 8–12 h at 4 °C. Following this step, Bio-beads (Bio-Rad) were added (typically 10 g for each 50 mL) and incubated with the sample for 24 h at 4 °C to remove LMNG detergent. The sample was then purified by SEC using a Superdex 200 10/300 column (Cytiva) preequilibrated with SEC buffer set to pH 5.0 (50 mM sodium acetate pH 5.0 and 400 mM NaCl) or pH 7.5 (20 mM Tris pH 7.5 and 400 mM NaCl). Peak fractions of the target protein were pooled and concentrated using a concentrator with a 10-kDa nominal cutoff molecular weight (Millipore).

Cryo-EM sample preparation and screening

NorA-BRIL^{3A} cryo-EM samples were prepared in the absence (pH 7.5) or the presence of 3-fold molar excesses of BAG2 (pH 5.0) or BAG2 and Fab36 (pH 7.5) by incubating for 1 h at 4 °C. Each sample was purified with SEC using a Superdex 200 10/300 column (Cytiva) pre-equilibrated with SEC buffer set to pH 5.0 (50 mM sodium acetate pH 5.0 and 400 mM NaCl) or pH 7.5 (20 mM Tris pH 7.5 and 400 mM NaCl).

NorA-BRIL^{1A} cryo-EM samples were prepared in the absence (pH 7.5) or the presence of 3-fold molar excesses of BAG2 and Fab36 (pH 7.5) by incubating for 1 h at 4 °C. Each sample was purified with SEC using a Superdex 200 10/300 column (Cytiva) preequilibrated with SEC buffer set pH 7.5 (20 mM Tris pH 7.5 and 400 mM NaCl). Note that we found the NorA-BRIL^{1A}-BAG2-Fab36 sample to possess few intact complexes where NorA-BRIL^{1A} was bound to both BAG2 and Fab36. Therefore, NorA-BRIL^{1A}-BAG2 particles from this sample were used to compare with NorA-BRIL^{3A} particles at pH 7.5.

To prepare cryo-EM grids, 3.8 µL of sample at ~4 mg/mL was applied onto UltrAuFoil 300-mesh R1.2/1.3 grids (Quantifoil) that were glow-discharged with the PELCO easiGlow GlowDischarge system (Ted Pella Inc.). Grids were blotted on both sides for 3.5 or 4 s at 100% humidity and a temperature of 4 °C, and then plunge-frozen into liquid ethane (cooled by liquid nitrogen) using a FEI Vitrobot Mark IV. NorA-BRIL samples were screened on a Talos Arctica microscope (200 kV X-FEG electron source, two condenser lens system) equipped with a Gatan K3 camera (5760 × 4092). Notably, a small dataset for NorA-BRIL^{3A}-BAG2-Fab36 complex generated a Coulomb potential map at 3.63 Å with 73,813 particles. A slight preferred orientation problem was detected where side views were predominately captured and displayed more distinct helices than the top or bottom views in the two-dimensional classification. Thus, subsequent Krios data collection was imaged on tilted and untilted grids for this sample.

Cryo-EM data collection

Cryo-EM data for NorA-BRIL^{3A}-BAG2 and NorA-BRIL^{3A}-BAG2-Fab36 samples were acquired on a Titan EF-Krios microscope at 105,000x nominal magnification under 300 kV (imaging system: Gatan Bioquantum K3 camera)[80–82]. Zero-loss images were taken using a GIF-Quantum energy filter with a 20 eV slit. Leginon software version 3.6 was used for automated data collection[83]. Movies were collected with a physical pixel size of 0.413 Å (dose fractioned over 60 frames for tilted micrographs and 40 frames for non-tilted micrographs). The NorA-BRIL^{3A}-BAG2 and NorA-BRIL^{3A}-BAG2-Fab36 datasets received an

accumulated dose of 48.53 $e^-/Å^2$ and 48.61 $e^-/Å^2$, respectively. The ice thickness *on-the-fly* was measured to select the holes with the desired ice thickness for data collection[82]. A total of 10,267 movies were collected for NorA-BRIL^{3A}-BAG2 at a nominal defocus range of −0.6 – 2.5 µm, and 5,543 movies (1,294 tilted and 4,249 untilted) were collected for NorA-BRIL^{3A}-BAG2-Fab36 at a nominal defocus range of −0.5 to −2.5 µm[84,85]. On-the-fly movie processing was executed using MotionCor2 software version 1.5 and CTFFIND4 software version 4.1.13, under regulatory purview of Appion[85,86]. Meanwhile, on-the-fly particle picking was performed using Warp[87].

Cryo-EM image processing and map analysis

The NorA-BRIL^{3A}-BAG2 and NorA-BRIL^{3A}-BAG2-Fab36 datasets were processed in cryoSPARC (version 3.3.1)[88] with similar steps. The patch contrast transfer function was estimated for the dose-weighted micrographs. Initial 2D class averages were generated using particles picked by Warp[87]. Topaz training[89] and template-based picking were used for additional rounds of particle picking. A total of 5.29 and 4.03 million particles were selected from the NorA-BRIL^{3A}-BAG2 and NorA-BRIL^{3A}-BAG2-Fab36 datasets, respectively. Particles underlying well-resolved 2D classes were used for initial ab initio model building, and all picked particles were used for subsequent heterogenous three-dimensional (3D) refinement. Particles from classes corresponding to complete NorA-BRIL^{3A}-BAG2 and NorA-BRIL^{3A}-BAG2-Fab36 complexes or complexes apparently lacking the Fab constant domain were retained for subsequent rounds of ab initio model building and heterogeneous 3D classification. After multiple rounds, a non-uniform 3D refinement step was used to generate the final 3.21 Å (159,621 particles), 3.18 Å (117,232 particles), and 3.25 Å (184,707 particles) resolution maps of NorA-BRIL^{3A}-BAG2 in the inward-open, inward-occluded, and occluded conformations, as assessed using the gold standard Fourier shell correlation (FSC) at FSC = 0.143[90], where the final number of particles underlying the cryo-EM map are given in the parentheses. Likewise, the final 2.56 Å (298,088 particles) resolution map of NorA-BRIL^{3A}-BAG2-Fab36 in the outward-open conformation was assessed using the same gold standard FSC. Directional FSC distribution and angular particle distribution heat maps show little preferred orientation bias for both complexes. Particles were evenly distributed with various orientations that generated 2D classes of similar resolution. Final maps were sharpened using Phenix.auto_sharpen for 3D model building[91].

Structural model refinement

Structural models of the complexes were built and refined in Coot[92] and Phenix[91], respectively. The NorA-Fab36 structure (PDB ID: 7LO8) was used as the reference structure for initiating model building from the cryo-EM map obtained for the NorA-BRIL^{3A}-BAG2-Fab36 sample at pH 7.5. The AlphaFold2 predicted structure of NorA-BRIL^{3A} and the crystal structure of BAG2 (PDB ID: 6CBV) were used as starting reference structures for initiating model building from the cryo-EM map obtained for the NorA-BRIL^{3A}-BAG2 sample at pH 5.0.

Growth inhibition assay in E. coli

C43 (DE3) *E. coli* cells were transformed with NorA in pET28, NorA-BRIL^{3A} in pET29a, and a control dead NorA mutant in pET28 (i.e., E222Q/D307N) and grown on Luria-Bertani (LB) agar plates infused with 100 µg/mL kanamycin. Next, a single colony was inoculated into LB liquid culture supplemented with 20 µM IPTG and 100 µg/mL kanamycin and grown overnight at 37 °C. Overnight cultures were diluted by 200-fold in fresh LB media supplemented with 20 µM IPTG, 100 µg/mL kanamycin, and different norfloxacin concentrations ranging from 0 to 1.6 µg/mL. OD_{600nm} was monitored over time using a BioScreen Pro C device at 30 °C with shaking between measurements every 15 min. Similar results were obtained in at least two independent experiments.

Bioinformatic analysis of MFS transporters

A total of 1,118 MFS transporters were analyzed from the Transporter Classification Database[63]. The corresponding AlphaFold2 model for each of the above Uniprot IDs was analyzed to identify the last residue in the terminal TM domain helix using the biopython "DSSP" module. Each of these residues was manually checked to ensure the residue was in the desired location. The i + 1 residue relative to the last helical one and subsequent residues along with their pDLLT scores from the AlphaFold2 were used for subsequent analysis. The list of MFS transporter Uniprot IDs is provided in the Supplementary Material.

GlpT-BRIL^{0A}, Bmr-BRIL^{7A} and Blt-BRIL^{7A} construct expression and purification

The GlpT-BRIL^{0A} gene, corresponding to residues Met1 to Arg441 of GlpT, was purchased (Twist Biosciences) and cloned in a modified pBAD33 vector[93] between EcorI and XbaI cut sites (the fusion protein sequence is listed in Supplementary Table 3). The C-terminus following BRIL contained a TEV cleavage site, a myc tag, and a 10x His-tag. The plasmid was transformed into C43(DE3) *E. coli* and a starter overnight 100 mL LB growth was inoculated and grown at 37 °C. In the morning, 10 mL of overnight culture was added to each of six baffled flasks containing 1 L LB. The culture was grown at 37 °C to an OD_{600nm} of ~1.0, upon which the temperature was reduced to 25 °C. After 30 min, the culture was induced with 0.1% arabinose and expressed for 1.5 h, similar to a prior study on GlpT[94]. Cell pellets were harvested by centrifugation and immediately lysed in buffer (50 mM Tris pH 8.0, 400 mM NaCl, 10% glycerol, 1 mM EDTA) containing protease inhibitors (0.5 µg/ml pepstatin A (w/v), 0.5 µg/ml leupeptin (w/v), 0.5 µg/ml E-64 (w/v), 0.5 mM PMSF) at a ratio of 5 mL buffer per gram of cells. The suspension was passed five times through an EmulsiFlex-C3 high pressure homogenizer (Avestin, Inc.) for lysis. Next, the lysate was centrifuged at 13,000 x g for 20 min at 4 °C in a Beckman centrifuge equipped with a JA-25.50 rotor (Beckman Coulter). The supernatant was further centrifuged at 40,000 r.p.m. (186,386 x g, maximum) for 2.5 h at 4 °C using a Beckman ultracentrifuge equipped with a Type 45 Ti fixed-angle rotor (Beckman Coulter) to purify the membrane fraction. The pellet was suspended in membrane buffer (20 mM Tris pH 8.0, 300 mM NaCl, 10% glycerol, 10 mM imidazole, 1% (w/v) dodecyl-β-D-maltopyranoside (DDM; Anatrace)) at a ratio of 10 mL buffer per gram of membrane. The suspension was stirred for 2 h at 4 °C and subsequently centrifuged at 35,000 r.p.m. (142,688 x g, maximum) for 30 min at 4 °C using a Beckman ultracentrifuge equipped with a Type 45 Ti fixed-angle rotor (Beckman Coulter) to remove insoluble material. The supernatant was incubated with ~1 mL Ni-NTA resin (Thermo Fisher Scientific) and gently stirred at 4 °C for 2 h. This suspension was loaded onto a column, washed with wash buffer (20 mM Tris pH 8.0, 200 mM NaCl, 10% glycerol, 25 mM imidazole, 0.2% DDM), and eluted with elution buffer (20 mM Tris pH 7.5, 200 mM NaCl, 10% glycerol, 400 mM imidazole, 0.2% DDM). Fractions containing GlpT-BRIL^{0A} were pooled and cleaved overnight with TEV protease at 4 °C. The next morning, the sample was dialyzed for 2 h in dialysis buffer (20 mM Tris pH 7.5, 100 mM NaCl) and subsequently stirred with Ni-NTA resin for 1 h at 4 °C. This suspension was loaded onto a column and the flow through collected. PMAL-C8 amphipol (Anatrace) was added to the flow through fractions at a 5/1 ratio (w/w) of PMAL-C8/GlpT-BRIL^{0A} and incubated with stirring for 16 h at 4 °C. Next, bio-beads (Bio-Rad) were added (typically 10 g for each 50 mL) and incubated with the sample for 24 h at 4 °C to remove DDM detergent. Finally, the sample was purified by SEC using a Superdex 200 10/300 column (Cytiva) pre-equilibrated with SEC buffer (20 mM Tris pH 7.5 and 100 mM NaCl). Purified fractions were used for binding to BAG2 which is described below.

The Bmr-BRIL^{7A} and Blt-BRIL7A genes were purchased (Twist Biosciences) and cloned in a pET29 vector, similar to NorA (the fusion protein sequences are listed in Supplementary Table 3). The growth of

the Bmr and Blt fusion proteins were identical to those of NorA with the use of autoinduction media and C43(DE3) *E. coli*, as previously described above[18]. Cell pellets were thawed, resuspended, and homogenized in lysis buffer (40 mM Tris pH 8.0, 400 mM NaCl, 10% glycerol), and centrifuged at 6,000 x g for 20 min at 4 °C in a Beckman centrifuge equipped with a JA-25.50 rotor (Beckman Coulter). The membrane fractions were isolated by centrifugation for 4 h at 35,000 r.p.m. (142,688 x g, maximum) using a Beckman ultracentrifuge equipped with a Type 45 Ti fixed-angle rotor (Beckman Coulter). Subsequently, membrane factions were solubilized in buffer (20 mM Tris pH 8.0, 400 mM NaCl, 10% glycerol (v/v), 10 mM imidazole, 1% (w/v) lauryl maltose neopentyl glycol (LMNG; Anatrace)) for 1 h at 4 °C. The detergent insoluble fraction was removed by centrifuging at 35,000 r.p.m. (142,688 x g, maximum) for 30 min at 4 °C. Nickel affinity resin (Thermo Fisher Scientific) was added to solubilized membrane fractions and incubated at 4 °C for 1-2 h. After washing away unwanted proteins with wash buffer (20 mM Tris pH 8.0, 200 mM NaCl, 10% glycerol (v/v), 0.2% (w/v) LMNG, 25 mM imidazole), fusion proteins were eluted with a similar buffer containing 400 mM imidazole. Subsequently, the C-terminal 10x-His tags were removed by incubation with TEV protease at 4 °C for 16 h and subsequently dialyzed into dialysis buffer (20 mM Tris pH 7 and 100 mM NaCl). The mixture for each construct was passed over a Ni-NTA column to separate Bmr-BRIL^{7A} and Blt-BRIL^{7A} proteins present in the flow through from TEV captured in the affinity resin. Fractions containing the fusion proteins were incubated with PMAL-C8 amphipol (Anatrace) at a 5/1 ratio (w/w) of PMAL-C8/fusion protein for 16 h at 4 °C. Following this incubation, Bio-beads (Bio-Rad) were added (typically 10 g for each 50 mL) and incubated with the sample for 24 h at 4 °C to remove LMNG detergent. The sample was then purified by SEC using a Superdex 200 10/300 column (Cytiva) preequilibrated with SEC buffer (20 mM sodium phosphate pH 5.0 and 100 mM NaCl).

For SEC binding experiments, GlpT-BRIL^{0A}, Bmr-BRIL^{7A}, and Blt-BRIL^{7A} alone and in the presence of 3-fold molar excess BAG2 were injected into Superdex 200 10/300 column (Cytiva) preequilibrated with SEC buffer (20 mM Tris pH 7.5 and 100 mM NaCl).

Cryo-EM experiments on GlpT-BRIL^{0A}, Bmr-BRIL^{7A}, and Blt-BRIL^{7A} bound with BAG2

GlpT-BRIL^{0A}, Bmr-BRIL^{7A}, and Blt-BRIL^{7A} cryo-EM samples were prepared in the presence of 3-fold molar excesses of BAG2 at pH 7.5 for the GlpT sample and at pH 5.0 for Bmr and Blt samples. Each sample was purified with SEC using a Superdex 200 10/300 column (Cytiva) preequilibrated with SEC buffer set to the respective pH value: (i) 20 mM Tris pH 7.5 and 100 mM NaCl for GlpT-BRIL^{0A}, (ii) 20 mM phosphate pH 5.0 and 100 mM NaCl for Bmr-BRIL^{7A}, and (iii) 50 mM sodium acetate pH 5.0 and 100 mM NaCl for Blt-BRIL^{7A}.

To prepare cryo-EM grids, 4 µL of SEC purified complexes at ~2–4 mg/mL of the GlpT-BRIL^{0A}, Bmr-BRIL^{7A}, and Blt-BRIL^{7A} were applied onto UltrAuFoil 300-mesh R1.2/1.3 grids (Quantifoil) that were glow-discharged with the PELCO easiGlow Glow Discharge system (Ted Pella Inc.). Grids were blotted on both sides for 3 or 3.5 s at 100% humidity and 16 °C, and then plunge-frozen into liquid ethane (cooled by liquid nitrogen) using a FEI Vitrobot Mark IV. Samples were screened on a Talos Arctica microscope (200 kV X-FEG electron source, two condenser lens system) equipped with a Gatan K3 camera (5760 × 4092).

Reporting summary

Further information on research design is available in the Nature Portfolio Reporting Summary linked to this article.

Data availability

The cryo-EM maps have been deposited in the Electron Microscopy Data Bank (EMDB) under accession codes EMD-44145 (NorA in the inward-open conformation; NorA-BRIL^{3A}-BAG2 sample at pH 5.0), EMD-44147 (NorA in the inward-occluded conformation; NorA-BRIL^{3A}-BAG2 sample at pH 5.0), EMD-44144 (NorA in the occluded conformation; NorA-BRIL^{3A}-BAG2 sample at pH 5.0), and EMD-44143 (NorA in the outward-open conformation; NorA-BRIL^{3A}-BAG2-Fab36 sample at pH 7.5). The atomic coordinates have been deposited in the Protein Data Bank (PDB) under accession codes 9B3M (NorA in the inward-open conformation; NorA-BRIL^{3A}-BAG2 sample at pH 5.0), 9B3O (NorA in the inward-occluded conformation; NorA-BRIL^{3A}-BAG2 sample at pH 5.0), 9B3L (NorA in the occluded conformation; NorA-BRIL^{3A}-BAG2 sample at pH 5.0), and 9B3K (NorA in the outward-open conformation; NorA-BRIL^{3A}-BAG2-Fab36 sample at pH 7.5). Previously published structures discussed or analyzed in this work are as follows: 7LO8 and 6CBV. Source data are provided with this paper.

References

1. Kühlbrandt, W. Biochemistry. The resolution revolution. *Science* **343**, 1443–1444 (2014).
2. De Zorzi, R., Mi, W., Liao, M. & Walz, T. Single-particle electron microscopy in the study of membrane protein structure. *Microscopy* **65**, 81–96 (2016).
3. Fernandez-Leiro, R. & Scheres, S. H. Unravelling biological macromolecules with cryo-electron microscopy. *Nature* **537**, 339–346 (2016).
4. Kühlbrandt, W. Forty years in cryoEM of membrane proteins. *Microscopy* **71**, i30–i50 (2022).
5. Robertson, M. J., Meyerowitz, J. G. & Skiniotis, G. Drug discovery in the era of cryo-electron microscopy. *Trends Biochem. Sci.* **47**, 124–135 (2022).
6. Scheres, S. H. W., Ryskeldi-Falcon, B. & Goedert, M. Molecular pathology of neurodegenerative diseases by cryo-EM of amyloids. *Nature* **621**, 701–710 (2023).
7. Henderson, R. The potential and limitations of neutrons, electrons and X-rays for atomic resolution microscopy of unstained biological molecules. *Q Rev. Biophys.* **28**, 171–193 (1995).
8. Cheng, Y. Single-particle Cryo-EM at crystallographic resolution. *Cell* **161**, 450–457 (2015).
9. Herzik, M. A. Jr, Wu, M. & Lander, G. C. High-resolution structure determination of sub-100 kDa complexes using conventional cryo-EM. *Nat. Commun.* **10**, 1032 (2019).
10. D'Imprima, E. & Kuhlbrandt, W. Current limitations to high-resolution structure determination by single-particle cryoEM. *Q Rev. Biophys.* **54**, e4 (2021).
11. Harrison, P. J., Vecerkova, T., Clare, D. K. & Quigley, A. A review of the approaches used to solve sub-100 kDa membrane proteins by cryo-electron microscopy. *J. Struct. Biol.* **215**, 107959 (2023).
12. Wentinck, K., Gogou, C. & Meijer, D. H. Putting on molecular weight: enabling cryo-EM structure determination of sub-100 kDa proteins. *Curr. Res Struct. Biol.* **4**, 332–337 (2022).
13. Piper, S. J., Johnson, R. M., Wootten, D. & Sexton, P. M. Membranes under the magnetic lens: a dive into the diverse world of membrane protein structures using Cryo-EM. *Chem. Rev.* **122**, 13989–14017 (2022).
14. Bloch, J. S. et al. Development of a universal nanobody-binding Fab module for fiducial-assisted cryo-EM studies of membrane proteins. *Proc. Natl Acad. Sci. USA* **118**, e2115435118 (2021).
15. Sauer, D. B. et al. Structural basis for the reaction cycle of DASS dicarboxylate transporters. *Elife* **9**, e61350 (2020).
16. Wu, S. et al. Fabs enable single particle cryoEM studies of small proteins. *Structure* **20**, 582–592 (2012).
17. Nygaard, R., Kim, J. & Mancia, F. Cryo-electron microscopy analysis of small membrane proteins. *Curr. Opin. Struct. Biol.* **64**, 26–33 (2020).

18. Brawley, D. N. et al. Structural basis for inhibition of the drug efflux pump NorA from *Staphylococcus aureus*. *Nat. Chem. Biol.* **18**, 706–712 (2022).
19. Kim, J. et al. Structure and drug resistance of the *Plasmodium falciparum* transporter PfCRT. *Nature* **576**, 315–320 (2019).
20. Chen, Q. et al. Structures of rhodopsin in complex with G-protein-coupled receptor kinase 1. *Nature* **595**, 600–605 (2021).
21. Gusach, A., Garcia-Nafria, J. & Tate, C. G. New insights into GPCR coupling and dimerisation from cryo-EM structures. *Curr. Opin. Struct. Biol.* **80**, 102574 (2023).
22. Guo, Q. et al. A method for structure determination of GPCRs in various states. *Nat. Chem. Biol.* **20**, 74–82 (2024).
23. Zhang, K., Wu, H., Hoppe, N., Manglik, A. & Cheng, Y. Fusion protein strategies for cryo-EM study of G protein-coupled receptors. *Nat. Commun.* **13**, 4366 (2022).
24. Kwon, N. Y., Kim, Y. & Lee, J. O. The application of helix fusion methods in structural biology. *Curr. Opin. Struct. Biol.* **60**, 110–116 (2020).
25. Wang, Y. et al. Transport and inhibition mechanism for VMAT2-mediated synaptic vesicle loading of monoamines. *Cell Res.* **34**, 47–57 (2024).
26. Chu, R. et al. Redesign of a four-helix bundle protein by phage display coupled with proteolysis and structural characterization by NMR and X-ray crystallography. *J. Mol. Biol.* **323**, 253–262 (2002).
27. Chun, E. et al. Fusion partner toolchest for the stabilization and crystallization of G protein-coupled receptors. *Structure* **20**, 967–976 (2012).
28. Liu, W. et al. Structural basis for allosteric regulation of GPCRs by sodium ions. *Science* **337**, 232–236 (2012).
29. Wang, C. et al. Structural basis for smoothened receptor modulation and chemoresistance to anticancer drugs. *Nat. Commun.* **5**, 4355 (2014).
30. Cheng, R. K. Y. et al. Structural insight into allosteric modulation of protease-activated receptor 2. *Nature* **545**, 112-+ (2017).
31. Asada, H. et al. Crystal structure of the human angiotensin II type 2 receptor bound to an angiotensin II analog. *Nat. Struct. Mol. Biol.* **25**, 570–576 (2018).
32. Kimura, K. T. et al. Structures of the 5-HT(2A) receptor in complex with the antipsychotics risperidone and zotepine. *Nat. Struct. Mol. Biol.* **26**, 121–128 (2019).
33. Zhou, Y., Cao, C., He, L., Wang, X. & Zhang, X. C. Crystal structure of dopamine receptor D4 bound to the subtype selective ligand, L745870. *Elife* **8**, e48822 (2019).
34. Mukherjee, S. et al. Synthetic antibodies against BRIL as universal fiducial marks for single-particle cryoEM structure determination of membrane proteins. *Nat. Commun.* **11**, 1598 (2020).
35. Miyagi, H. et al. The discovery of a new antibody for BRIL-fused GPCR structure determination. *Sci. Rep.* **10**, 11669 (2020).
36. Kern, D. M. et al. Structural basis for assembly and lipid-mediated gating of LRRC8A:C volume-regulated anion channels. *Nat. Struct. Mol. Biol.* **30**, 841–852 (2023).
37. Lyu, Y. et al. Engineering of a mammalian VMAT2 for cryo-EM analysis results in non-canonical protein folding. *Nat. Commun.* **15**, 6511 (2024).
38. Dang, Y. et al. Molecular mechanism of substrate recognition by folate transporter SLC19A1. *Cell Discov.* **8**, 141 (2022).
39. Tsutsumi, N. et al. Structure of human Frizzled5 by fiducial-assisted cryo-EM supports a heterodimeric mechanism of canonical Wnt signaling. *Elife* **9**, e58464 (2020).
40. Chen, H., Huang, W. & Li, X. Structures of oxysterol sensor EBI2/GPR183, a key regulator of the immune response. *Structure* **30**, 1016–1024.e1015 (2022).
41. Choi, C. et al. Understanding the molecular mechanisms of odorant binding and activation of the human OR52 family. *Nat. Commun.* **14**, 8105 (2023).
42. Lees, J. A. et al. An inverse agonist of orphan receptor GPR61 acts by a G protein-competitive allosteric mechanism. *Nat. Commun.* **14**, 5938 (2023).
43. Castells-Graells, R. et al. Cryo-EM structure determination of small therapeutic protein targets at 3 A-resolution using a rigid imaging scaffold. *Proc. Natl Acad. Sci. USA* **120**, e2305494120 (2023).
44. Yeates, T. O., Agdanowski, M. P. & Liu, Y. Development of imaging scaffolds for cryo-electron microscopy. *Curr. Opin. Struct. Biol.* **60**, 142–149 (2020).
45. Dutka, P. et al. Development of "plug and play" fiducial marks for structural studies of GPCR signaling complexes by single-particle Cryo-EM. *Structure* **27**, 1862–1874.e1867 (2019).
46. Wu, D. et al. Transport and inhibition mechanisms of human VMAT2. *Nature* **626**, 427–434 (2024).
47. Youn, S. J. et al. Construction of novel repeat proteins with rigid and predictable structures using a shared helix method. *Sci. Rep.* **7**, 2595 (2017).
48. Jumper, J. et al. Highly accurate protein structure prediction with AlphaFold. *Nature* **596**, 583–589 (2021).
49. Pao, S. S., Paulsen, I. T. & Saier, M. H. Major facilitator superfamily. *Microbiol Mol. Biol. R.* **62**, 1 (1998).
50. Drew, D., North, R. A., Nagarathinam, K. & Tanabe, M. Structures and general transport mechanisms by the major facilitator superfamily (MFS). *Chem. Rev.* **121**, 5289–5335 (2021).
51. Law, C. J., Maloney, P. C. & Wang, D. N. Ins and outs of major facilitator superfamily antiporters. *Annu Rev. Microbiol* **62**, 289–305 (2008).
52. Ng, E. Y., Trucksis, M. & Hooper, D. C. Quinolone resistance mediated by norA: physiologic characterization and relationship to flqB, a quinolone resistance locus on the *Staphylococcus aureus* chromosome. *Antimicrob. Agents Chemother.* **38**, 1345–1355 (1994).
53. Neyfakh, A. A., Borsch, C. M. & Kaatz, G. W. Fluoroquinolone resistance protein NorA of *Staphylococcus aureus* is a multidrug efflux transporter. *Antimicrob. Agents Chemother.* **37**, 128–129 (1993).
54. Li, J. et al. Proton-coupled transport mechanism of the efflux pump NorA. *Nat. Commun.* **15**, 4494 (2024).
55. Lyu, P. C., Liff, M. I., Marky, L. A. & Kallenbach, N. R. Side chain contributions to the stability of alpha-helical structure in peptides. *Science* **250**, 669–673 (1990).
56. O'Neil, K. T. & DeGrado, W. F. A thermodynamic scale for the helix-forming tendencies of the commonly occurring amino acids. *Science* **250**, 646–651 (1990).
57. Padmanabhan, S., Marqusee, S., Ridgeway, T., Laue, T. M. & Baldwin, R. L. Relative helix-forming tendencies of nonpolar amino acids. *Nature* **344**, 268–270 (1990).
58. Huang, Y., Lemieux, M. J., Song, J., Auer, M. & Wang, D. N. Structure and mechanism of the glycerol-3-phosphate transporter from *Escherichia coli*. *Science* **301**, 616–620 (2003).
59. Li, J., Sae Her, A. & Traaseth, N. J. Asymmetric protonation of glutamate residues drives a preferred transport pathway in EmrE. *Proc. Natl Acad. Sci. USA* **118**, e2110790118 (2021).
60. Gayen, A., Leninger, M. & Traaseth, N. J. Protonation of a glutamate residue modulates the dynamics of the drug transporter EmrE. *Nat. Chem. Biol.* **12**, 141–145 (2016).
61. Akyuz, N., Altman, R. B., Blanchard, S. C. & Boudker, O. Transport dynamics in a glutamate transporter homologue. *Nature* **502**, 114–118 (2013).
62. Fitzgerald, G. A. et al. Quantifying secondary transport at single-molecule resolution. *Nature* **575**, 528–534 (2019).
63. Saier, M. H. et al. The transporter classification database (TCDB): 2021 update. *Nucleic acids Res.* **49**, D461–D467 (2021).
64. Guo, H. B. et al. AlphaFold2 models indicate that protein sequence determines both structure and dynamics. *Sci. Rep.* **12**, 10696 (2022).

65. Woolridge, D. P. et al. Efflux of the natural polyamine spermidine facilitated by the Bacillus subtilis multidrug transporter Blt. *J. Biol. Chem.* **272**, 8864–8866 (1997).
66. Klyachko, K. A., Schuldiner, S. & Neyfakh, A. A. Mutations affecting substrate specificity of the *Bacillus subtilis* multidrug transporter Bmr. *J. Bacteriol.* **179**, 2189–2193 (1997).
67. Du, D. et al. Multidrug efflux pumps: structure, function and regulation. *Nat. Rev. Microbiol* **16**, 523–539 (2018).
68. Nikaido, H. & Pages, J. M. Broad-specificity efflux pumps and their role in multidrug resistance of gram-negative bacteria. *FEMS Microbiol Rev.* **36**, 340–363 (2012).
69. Law, C. J., Enkavi, G., Wang, D. N. & Tajkhorshid, E. Structural basis of substrate selectivity in the glycerol-3-phosphate: phosphate antiporter GlpT. *Biophys. J.* **97**, 1346–1353 (2009).
70. Holman, G. D. Structure, function and regulation of mammalian glucose transporters of the SLC2 family. *Pflug. Arch.* **472**, 1155–1175 (2020).
71. Prive, G. G. et al. Fusion proteins as tools for crystallization - the lactose permease from Escherichia-coli. *Acta Crystallogr D.* **50**, 375–379 (1994).
72. Liu, S. X. & Li, W. K. Protein fusion strategies for membrane protein stabilization and crystal structure determination. *Crystals* **12**, 1041 (2022).
73. McIlwain, B. C. et al. N-terminal transmembrane-helix epitope tag for x-ray crystallography and electron microscopy of small membrane proteins. *J. Mol. Biol.* **433**, 166909 (2021).
74. Collu, G. et al. Chimeric single alpha-helical domains as rigid fusion protein connections for protein nanotechnology and structural biology. *Structure* **30**, 95–106.e107 (2022).
75. Chen, H. W. et al. Structural and functional insights into Spns2-mediated transport of sphingosine-1-phosphate. *Cell* **186**, 2644-+ (2023).
76. Pidathala, S. et al. Mechanisms of neurotransmitter transport and drug inhibition in human VMAT2. *Nature* **623**, 1086–1092 (2023).
77. Wu, X. & Rapoport, T. A. Cryo-EM structure determination of small proteins by nanobody-binding scaffolds (Legobodies). *Proc. Natl Acad. Sci. USA* **118**, e2115001118 (2021).
78. Uchanski, T. et al. Megabodies expand the nanobody toolkit for protein structure determination by single-particle cryo-EM. *Nat. Methods* **18**, 60–68 (2021).
79. Bailey, L. J. et al. Locking the elbow: improved antibody fab fragments as chaperones for structure determination. *J. Mol. Biol.* **430**, 337–347 (2018).
80. Rheinberger, J., Oostergetel, G., Resch, G. P. & Paulino, C. Optimized cryo-EM data-acquisition workflow by sample-thickness determination. *Acta Crystallogr D. Struct. Biol.* **77**, 565–571 (2021).
81. Suloway, C. et al. Automated molecular microscopy: the new Leginon system. *J. Struct. Biol.* **151**, 41–60 (2005).
82. Rice, W. J. et al. Routine determination of ice thickness for cryo-EM grids. *J. Struct. Biol.* **204**, 38–44 (2018).
83. Cheng, A. et al. Leginon: New features and applications. *Protein Sci.* **30**, 136–150 (2021).
84. Zheng, S. Q. et al. MotionCor2: anisotropic correction of beam-induced motion for improved cryo-electron microscopy. *Nat. Methods* **14**, 331–332 (2017).
85. Rohou, A. & Grigorieff, N. CTFFIND4: Fast and accurate defocus estimation from electron micrographs. *J. Struct. Biol.* **192**, 216–221 (2015).
86. Lander, G. C. et al. Appion: an integrated, database-driven pipeline to facilitate EM image processing. *J. Struct. Biol.* **166**, 95–102 (2009).
87. Tegunov, D. & Cramer, P. Real-time cryo-electron microscopy data preprocessing with Warp. *Nat. Methods* **16**, 1146–1152 (2019).
88. Punjani, A., Rubinstein, J. L., Fleet, D. J. & Brubaker, M. A. cryoSPARC: algorithms for rapid unsupervised cryo-EM structure determination. *Nat. Methods* **14**, 290–296 (2017).
89. Bepler, T. et al. Positive-unlabeled convolutional neural networks for particle picking in cryo-electron micrographs. *Nat. Methods* **16**, 1153–1160 (2019).
90. Rosenthal, P. B. & Henderson, R. Optimal determination of particle orientation, absolute hand, and contrast loss in single-particle electron cryomicroscopy. *J. Mol. Biol.* **333**, 721–745 (2003).
91. Adams, P. D. et al. PHENIX: a comprehensive python-based system for macromolecular structure solution. *Acta Crystallogr D. Biol. Crystallogr.* **66**, 213–221 (2010).
92. Emsley, P. & Cowtan, K. Coot: model-building tools for molecular graphics. *Acta Crystallogr D. Biol. Crystallogr.* **60**, 2126–2132 (2004).
93. Jimenez, N. et al. Genetics and proteomics of *Aeromonas salmonicida* lipopolysaccharide core biosynthesis. *J. Bacteriol.* **191**, 2228–2236 (2009).
94. Auer, M. et al. High-yield expression and functional analysis of Escherichia coli glycerol-3-phosphate transporter. *Biochemistry* **40**, 6628–6635 (2001).
95. Pettersen, E. F. et al. UCSF Chimera-a visualization system for exploratory research and analysis. *J. Comput. Chem.* **25**, 1605–1612 (2004).

Acknowledgements

N.J.T. was supported by NIH (AI165782, AI108889) and NSF awards (MCB 1902449). D.N.W. was supported by NIH awards (R01NS108151, R01DK135088, R01AI165782 and R01GM121994) and grants from the G. Harold and Leila Y. Mathers Foundation and the TESS Research Foundation. We thank S. Koide for valuable comments about the manuscript, P. Mishra, B. Ramirez, and J. Li for helpful discussions, and G. Hocky and S. Wang for sharing a script to run AlphaFold2 software at the High Performance Computing (HPC) facility of NYU. Krios data collection and screening on the Talos Arctica was performed at NYU Langone Health's Cryo-Electron Microscopy Laboratory (RRID: SCR_019202), which is partially supported by the Laura and Isaac Perlmutter Cancer Center Support Grant NIH/NCI P30CA016087, where we acknowledge W. J. Rice and B. Wang for helpful discussions and assistance on data collection. Cryo-EM data processing used computing resources at the HPC facilities of NYU and NYU School of Medicine.

Author contributions

P.X. performed experiments related to the NorA-BRIL constructs: optimized expression and purification protocols, performed binding tests, prepared samples for cryo-EM, collected cryo-EM datasets, processed and analyzed cryo-EM datasets, refined atomic models, interpreted the structures, and wrote the manuscript. Y.L. performed experiments related to the NorA-BRIL constructs: froze grids for cryo-EM, collected cryo-EM datasets, and processed and analyzed cryo-EM datasets, including the NorA-BRIL^{3A}-BAG2 dataset resulting in the three cryo-EM maps and initial processing of the NorA-BRIL^{3A}-BAG2-Fab36 dataset at 2.58 Å resolution. G.L. performed growth inhibition experiments and experiments related to the Bmr-BRIL^{7A}, Blt-BRIL^{7A}, and GlpT-BRIL^{0A} constructs, including optimizing expression and purification protocols, performed binding tests, prepared samples for cryo-EM, froze grids for cryo-EM, collected cryo-EM datasets, and processed and analyzed cryo-EM datasets. H.K. collected cryo-EM datasets and guided dataset processing for NorA-BRIL datasets. D.N.W. directed the project. N.J.T. designed and directed the project and wrote the manuscript. All authors participated in data analysis and revision of the manuscript.

Competing interests

D.N.W. and N.J.T. are listed as inventors of a patent application filed by New York University on NorA inhibitors (WO2023014970A2). The other authors declare no competing interests.

Additional information

Supplementary information The online version contains supplementary material available at https://doi.org/10.1038/s41467-024-54986-5.

Correspondence and requests for materials should be addressed to Da-Neng Wang or Nathaniel J. Traaseth.

Peer review information *Nature Communications* thanks the anonymous reviewers for their contribution to the peer review of this work. A peer review file is available.